Cell Reports

Article

miR-449a/miR-340 reprogram cell identity and metabolism in fusion-negative rhabdomyosarcoma

Graphical abstract

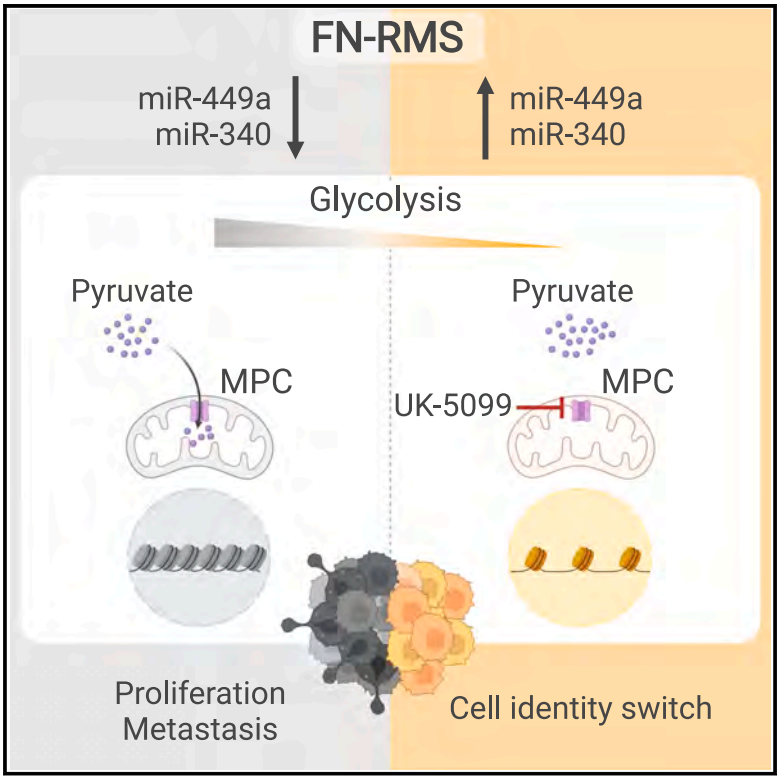

Authors

Enrico Pozzo, Laura Yedigaryan, Nefele Giarratana, ..., Sarah-Maria Fendt, Anne Uyttebroeck, Maurilio Sampaolesi

Correspondence

enrico.pozzo@kuleuven.be (E.P.), maurilio.sampaolesi@kuleuven.be (M.S.)

In brief

Pozzo et al. identify miR-449a and miR-340 as regulators of the FN-RMS cell cycle and p53 pathways. Multiomics analyses show that these miRNAs rewire cell identity and metabolism, reducing proliferation and metastatic potential; pharmacological MPC inhibition mirrors their impact in FN-RMS models.

Highlights

- miR-449a/miR-340 downregulation in FN-RMS targets cell cycle, histone, and glycolysis pathways
- miRNA reintroduction alters cell identity, impacting transcriptome, epigenome, and metabolism
- MPC inhibition or miR-449a/miR-340 drive cell cycle exit, reducing FN-RMS metastatic potential

Pozzo et al., 2025, Cell Reports *44*, 115171
January 28, 2025
https://doi.org/10.1016/j.celrep.2024.115171

CellPress

Cell Reports

CellPress
OPEN ACCESS

Article

miR-449a/miR-340 reprogram cell identity and metabolism in fusion-negative rhabdomyosarcoma

Enrico Pozzo,[1,13,*] Laura Yedigaryan,[1,13] Nefele Giarratana,[1,13] Chao-chi Wang,[1] Gabriel Miró Garrido,[1] Ewoud Degreef,[1] Vittoria Marini,[1] Gianmarco Rinaldi,[2,3] Bernard K. van der Veer,[4] Gabriele Sassi,[1,5] Guy Eelen,[6] Mélanie Planque,[2,3] Alessandro Fanzani,[7] Kian Peng Koh,[4] Peter Carmeliet,[6,8,9] Jason T. Yustein,[10] Sarah-Maria Fendt,[2,3] Anne Uyttebroeck,[11] and Maurilio Sampaolesi[1,12,14,*]

[1]Translational Cardiomyology Laboratory, Stem Cell and Developmental Biology, Department of Development and Regeneration, KU Leuven, Herestraat 49, 3000 Leuven, Belgium
[2]Laboratory of Cellular Metabolism and Metabolic Regulation, VIB-KU Leuven Center for Cancer Biology, VIB, Herestraat 49, 3000 Leuven, Belgium
[3]Laboratory of Cellular Metabolism and Metabolic Regulation, Department of Oncology, KU Leuven and Leuven Cancer Institute (LKI), Herestraat 49, 3000 Leuven, Belgium
[4]Laboratory of Stem Cell and Developmental Epigenetics, Department of Development and Regeneration, KU Leuven, Herestraat 49, 3000 Leuven, Belgium
[5]Clinical and Experimental Endocrinology (CEE), KU Leuven, Herestraat 49, 3000 Leuven, Belgium
[6]Laboratory of Angiogenesis and Vascular Metabolism, Department of Oncology and Leuven Cancer Institute (LKI), KU Leuven, VIB Center for Cancer Biology, VIB, 3000 Leuven, Belgium
[7]Department of Molecular and Translational Medicine, University of Brescia, Brescia, Italy
[8]Center for Biotechnology, Khalifa University of Science and Technology, Abu Dhabi, United Arab Emirates
[9]Laboratory of Angiogenesis and Vascular Heterogeneity, Department of Biomedicine, Aarhus University, 8000 Aarhus, Denmark
[10]Aflac Cancer and Blood Disorders Center, Emory University, Atlanta, GA, USA
[11]Department of Pediatric Hemato-Oncology, University Hospitals Leuven, Herestraat 49, 3000 Leuven, Belgium
[12]Histology and Medical Embryology Unit, Department of Anatomy, Histology, Forensic Medicine and Orthopedics, Sapienza University of Rome, Rome, Italy
[13]These authors contributed equally
[14]Lead contact
*Correspondence: enrico.pozzo@kuleuven.be (E.P.), maurilio.sampaolesi@kuleuven.be (M.S.)
https://doi.org/10.1016/j.celrep.2024.115171

SUMMARY

Rhabdomyosarcoma (RMS), the most common pediatric soft tissue sarcoma, arises in skeletal muscle and remains in an undifferentiated state due to transcriptional and post-transcriptional regulators. Among its subtypes, fusion-negative RMS (FN-RMS) accounts for the majority of diagnoses in the pediatric population. MicroRNAs (miRNAs) are non-coding RNAs that modulate cell identity via post-transcriptional regulation of messenger RNAs (mRNAs). In this study, we identify miRNAs impacting FN-RMS cell identity, revealing miR-449a and miR-340 as major regulators of the cell cycle and p53 signaling. Through miR-eCLIP technology, we demonstrate that miR-449a and miR-340 directly target transcripts involved in glycolysis and mitochondrial pyruvate transport, inhibiting the mitochondrial pyruvate carrier (MPC) complex. Pharmacological MPC inhibition induces a similar metabolic shift, reducing metastatic potential and leading to cell cycle exit. Overall, miR-449 and miR-340 orchestrate FN-RMS cell identity, positioning MPC inhibition as a strategy to shift FN-RMS cells toward a non-tumorigenic, quiescent state.

INTRODUCTION

Rhabdomyosarcoma (RMS) is the most common soft tissue sarcoma in the pediatric population, with more than 50% of patients being under the age of 10.[1] RMS can be classified into either fusion-positive RMS (FP-RMS) or fusion-negative RMS (FN-RMS), with the latter being the most common histology. While FP-RMS is characterized by the expression of PAX3-FOXO1 or PAX7-FOXO1 chimeric fusion protein, FN-RMS mutations mainly include signal transduction pathways (especially rat sarcoma virus and phosphatidylinositol 3-kinase), cell cycle regulators, and the p53 pathway. Besides FN-RMS genomic instabilities, post-transcriptional regulators are also crucial in maintaining FN-RMS subpopulation heterogeneity.

MicroRNAs (miRNAs, miRs) are short non-coding RNAs that have a major role in physiological and pathological muscle states via post-transcriptional regulation of mRNA to degrade it or prevent its translation into proteins.[2,3] We have previously described

the effects of a pro-myogenic miRNA cocktail, miR-181a and miR-212,[4] identified by myogenic induction screening of induced pluripotent stem cells,[5] in a novel genetically engineered murine model of FN-RMS with phenotypic and molecular features similar to human RMS.[6]

We hypothesized that, by reintroducing deregulated patient-specific miRNAs in FN-RMS cell models, we would be able to commit the tumor to a non-tumorigenic state. Thus, we identified miR-449a and miR-340 as the two key downregulated miRNAs in FN-RMS targeting cell cycle and p53 signaling. By using miR-eCLIP technology, we identified the direct effects of the miRNAs in FN-RMS, with downstream effects at the transcriptional, epigenetic, and metabolic level. We observed the miRNA-mediated direct targeting of glycolysis with blockade of pyruvate entry into mitochondria. Use of the mitochondrial pyruvate complex (MPC) inhibitor UK-5099 showed a similar metabolic shift, with cell cycle exit and dramatic reduction in its metastatic potential. Overall, this study identifies a miRNA combination that is able to orchestrate the cell identity of FN-RMS, with the modulation of MPC as a key metabolic regulator.

RESULTS

Identification of key downregulated miRNAs

We aimed to identify deregulated miRNAs in patients with FN-RMS (i.e., absent in tumor and relevant for FN-RMS biology) and validate their effects in FN-RMS cell models with RNA sequencing (RNA-seq; see workflow in Figure 1A). Thus, we analyzed publicly available data of the miRNA signature of patients diagnosed with FN-RMS[7] (SRA: PRJNA326118) (Figure 1B). We identified the cell cycle and p53 signaling as the top upregulated pathways according to the downregulated miRNA signature in patients with FN-RMS using DIANA software[8] (Figure 1C). This aligns with the differentially expressed pathway analysis based on the dataset of RNA-seq of patients with FN-RMS compared with skeletal muscle[9] (GSE108022), which revealed the cell cycle and p53 signaling as the key upregulated pathways in FN-RMS (Figure 1D). By focusing on the miRNAs with the strongest experimental evidence for involvement in these two pathways using miRPathDB,[10] and excluding those not present in the miRNA signature of patients, we identified miR-449a (Figure 1E) and miR-340 (Figure 1F) as two key miRNAs that are downregulated in FN-RMS and are involved in the cell cycle and p53 signaling, respectively.

Effects of miRNA perturbation on the FN-RMS transcriptome and proliferation

We sought to understand the role of the selected miRNAs in FN-RMS. Thus, we transfected both human and mouse FN-RMS cell models with miR-449a and miR-340-5p. The transfection efficiency appeared to be above 70% in both FN-RMS cell models (Figure S1A), and a log-fold increase of at least 2 for both miRNAs after transfection was observed (Figure S1B). miR-449a appeared to induce cell cycle exit, as seen by a shift from S phase into G0/G1 phase with 5-ethynyl-2 deoxyuridine (EdU) (Figure 2A), while miR-340-5p showed downregulation of the genes related to the p53 pathway according to miRPathDB, including *CCND1*, *CCNG2*, and *MDM2*, with RT-qPCR (Figure 2B; primer sequences are listed in Table S1). When testing the effects of the miRNAs in a previously described co-culture system of FN-RMS and adult skeletal muscle cells,[4] we observed that miR-449a blocked cell proliferation in tumor cells but reduced the myogenic potential of skeletal muscle cells. Conversely, the use of miR-340 had a reduced effect on cell proliferation but aided skeletal muscle differentiation. The combination of the two miRNAs had an additive effect in blocking tumor cell proliferation and helping skeletal muscle differentiation (Figure 2C). Indeed, after miRNA transfection, there was a tangible effect in terms of a reduced number of cells only in FN-RMS but not in mesangioblasts (MABs) (Figure S1C). The cell cycle blockade effect was sustained with the combined miRNA treatment in both FN-RMS and FP-RMS cell lines (Figure S1D). When checking the effects of the combined miRNAs in other FN-RMS lines (human cell line, human tumoroids, and murine cell line), we observed an overall reduced number of cells (Figure S1E).

We then checked the perturbation effects of miR-449a+340 in FN-RMS at the transcriptome level by RNA-seq analysis. Both the principal-component analysis (Figures 2D and S2A) and the volcano plot (Figures 2E and S2B) showed a remarkable difference in miRNA-transfected human and murine FN-RMS cells compared to vehicle 60 h after transfection. By using g:Profiler, we checked the pathways that were enriched in the differentially expressed genes. When looking at the combined upregulated and downregulated genes, the two pathways involved after miRNA transfection were the cell cycle and p53 signaling (Figure 2F). By focusing separately on the upregulated and downregulated genes, the cilium appeared among the top upregulated pathways after miRNA perturbation, while the cell cycle was the key downregulated pathway (Figure S2C).

In order to untangle the transcriptomic heterogeneity of FN-RMS response to miRNA perturbation, we performed multiomics single-nucleus RNA-seq and assay for transposase-accessible chromatin with sequencing (snRNA-seq/ATAC-seq) 60 h after transfection (Figure S2D). On the uniform manifold approximation and projection of the snRNA-seq data, we observed a separation between cells that were transfected with miR-449a+340 and vehicle-treated FN-RMS cells (Figure 2G). Similar to the bulk RNA-seq, we observed upregulation of genes related to the cilium (as identified by van Dam et al.[12]) and downregulation of cell cycle genes also in the snRNA-seq (Figure S2E). Indeed, with miRNA perturbation, the cells increased the expression of markers of G1 phase[11] (Figure 2H).

Recent literature[13,14] has described the three differentiation states within FN-RMS; i.e., proliferating (“progenitor-like” according to DeMartino et al.,[13] “proliferative” according to Danielli et al.[14]), quiescent mesenchymal (“mesenchymal-like,” “progenitor”), and myogenic (“myoblast-like,” “differentiated”). To understand whether the reintroduction of miRNAs in FN-RMS would shift the cell identity, we crossed the genes used to characterize these three different states with the expressed genes in our snRNA-seq dataset (Figures S3A and S3B). The major effect was observed on the proliferating state, which appeared to characterize the targets downregulated by miRNAs. Conversely, miR-449a+340 appeared to increase the enrichment for genes of the quiescent mesenchymal state. Indeed, by crossing the overall expression of the target genes of miR-449a and

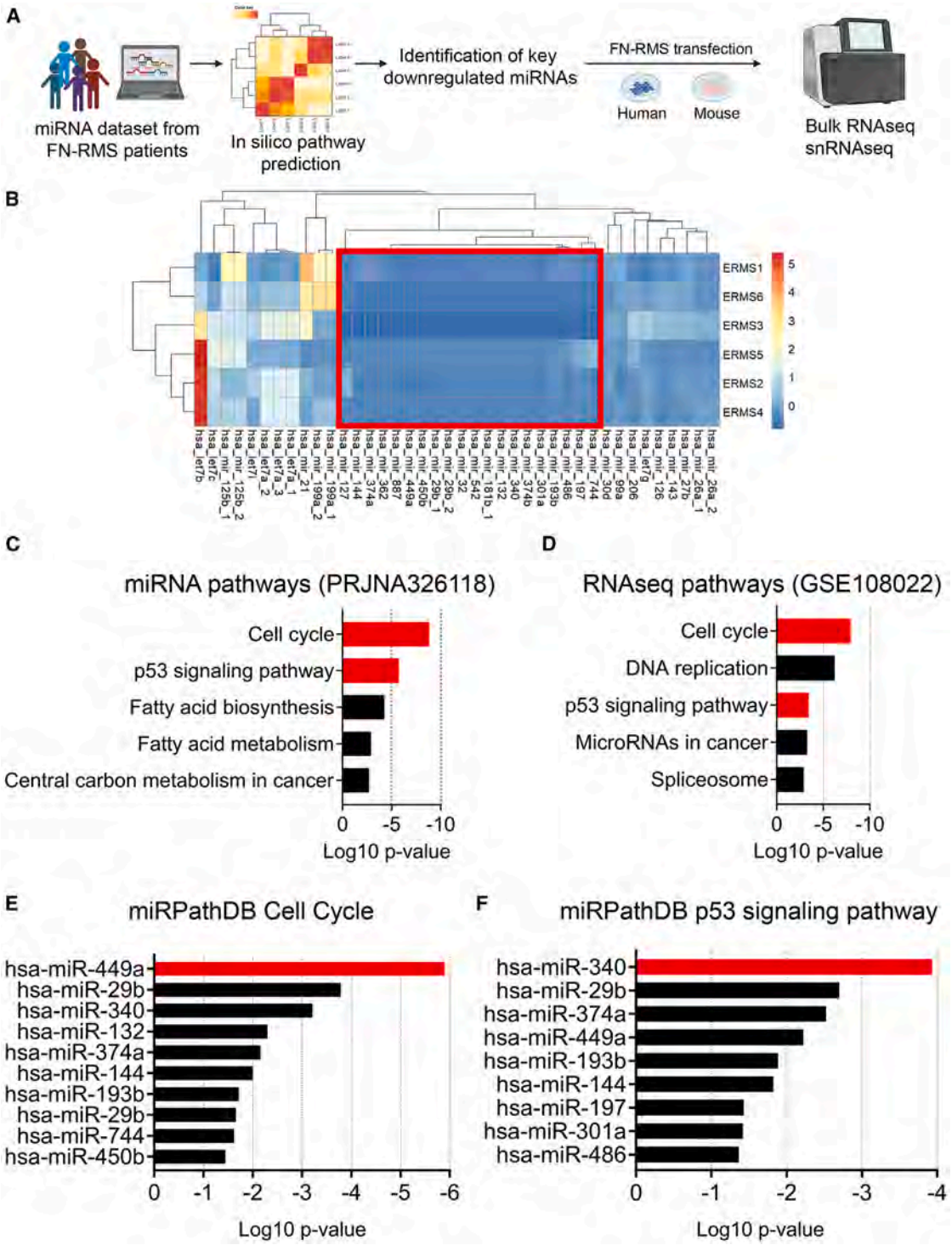

Figure 1. miRNA selection

(A) BioRender illustration showing a summary of the workflow.

(B) Selection of up- and downregulated miRNAs in patients with embryonal RMS (FN-RMS) (from PRJNA326118) (n = 6).

(C) Enriched pathways related to downregulated miRNAs, identified using DIANA software.

(D) Upregulated pathways from RNA-seq analysis of patients with FN-RMS compared to healthy skeletal muscle (66 patients, 5 skeletal muscles) (GSE108022).

(E and F) Top miRNAs downregulated in patients that target (E) the cell cycle pathway and (F) p53 signaling, according to miRPathDB.

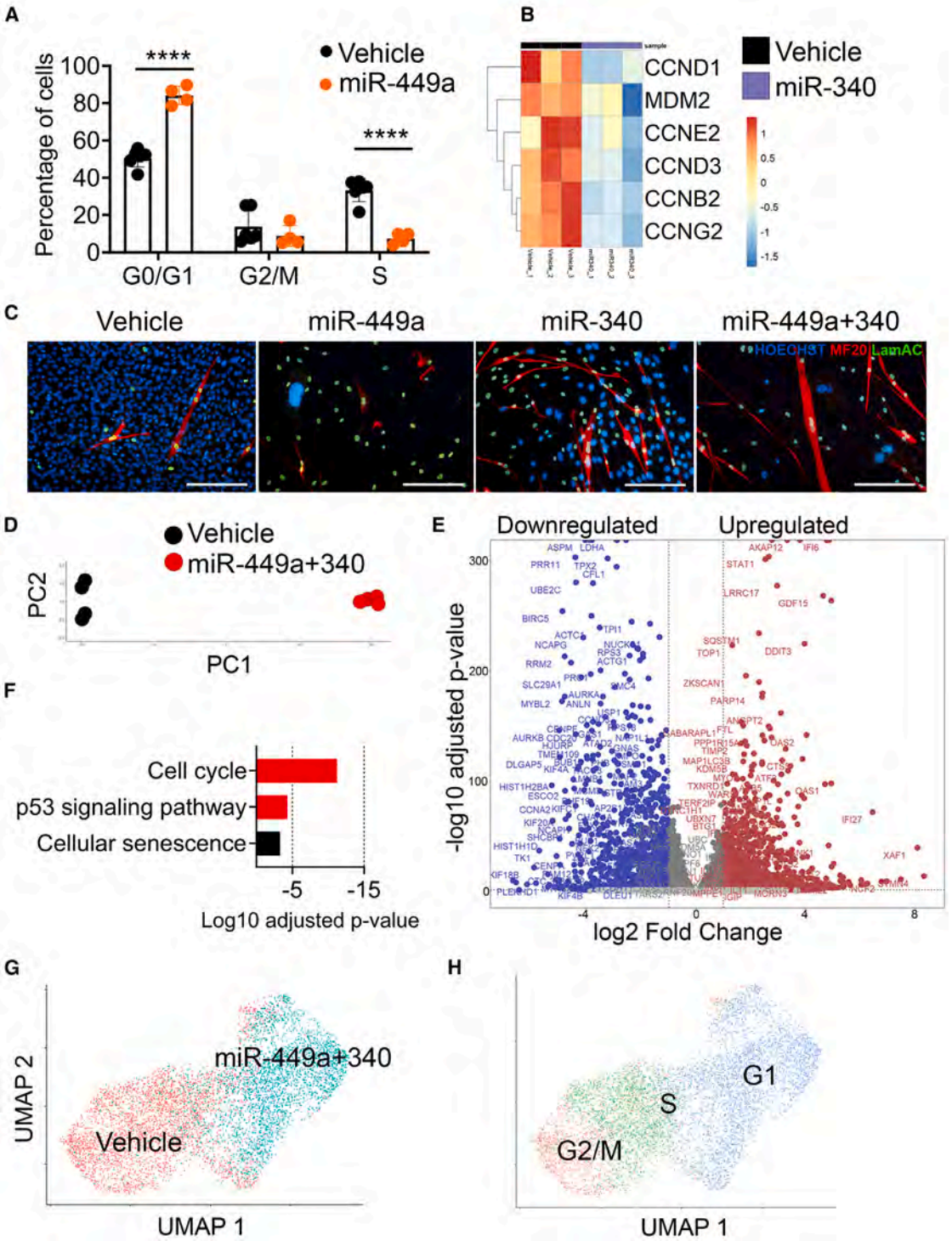

Figure 2. miR-449a and miR-340 effects

(A) EdU analysis of the FN-RMS cell line after miR-449a transfection ($n = 4$). Data are presented as mean ± SD, unpaired t test. ****$p < 0.0001$.

(B) Quantitative real-time PCR assessing the expression of genes involved in the p53 signaling pathway after miR-340-5p transfection ($n = 3$).

(C) Representative image of the co-culture system of murine FN-RMS and human MABs. Scale bar: 100 μm.

(legend continued on next page)

miR-340 with the patient dataset from DeMartino et al.,[13] increased expression of targeted genes was evident in the progenitor-like compared to mesenchymal-like subpopulation (Figure S3C). Wei et al.[15] described increased generation of tumorspheres in mesenchymal-like cells; thus, we similarly cultured FN-RMS under 3D conditions after transfection. Intriguingly, we observed a reduced sphere size in miRNA- compared to vehicle-treated FN-RMS (Figure S3D). Thus, it appears that the miR-449a+340 transfection shifts FN-RMS away from the proliferating state and toward a quiescent one (Figure S3E), with increased expression of genes related to the cilium, among many (Figure S3F).

Overall, the identified miRNAs demonstrate a significant impact on the transcriptome after transfection in FN-RMS cell lines, specifically influencing cell proliferation.

miR-449a+340 directly affect the cell cycle, metabolism, and histones in FN-RMS

In order to discern the direct and indirect targets leading to the observed effects, we captured trimeric miRNA-mRNA interactions using chimeric enhanced UV crosslinking and immunoprecipitation (chimeric eCLIP) (Figure 3A). Twenty-four hours after transfection, the abundance of the two miRNAs was confirmed (Figure S4A), with a similar percentage in chimeric peaks with seed match under both vehicle- and miRNA-transfected conditions (Figure S4B). An increase in the percentage of peaks targeted by miRNAs at the coding sequence was observed under miRNA conditions (Figure S4C). When looking at the different targets, overall, 708 targets appear to be directly targeted by the two miRNAs (Figure 3B), with miR-449a mainly affecting metabolism, proliferation, and chromatin organization (Figure 3C) and miR-340 predominantly influencing differentiation (Figure 3D). When combining the data from the direct targets of eCLIP with the bulk RNA-seq (nucleus+cytoplasm RNA) and snRNA-seq (nucleus RNA) performed 60 h after miRNA transfection (Figure S4D), it appeared that 40 direct targets were found in the nucleus sequencing (8 only in the nucleus, 32 both in the nucleus and cytoplasm) (Figure S5A), while 136 genes were targeted in the cytoplasm (Figure S5B).

Cell cycle- and p53-related genes (*CDK6*, *MDM4*, *MYC*, *CDK4*, *RHOA*, and *CCND1*), metabolism-related genes (*GAPDH*, *TXNIP*, *DDX5*, and *HIF1A*), and genes involved in histone modification (*H4C2*, *AEBP2*, *KAT6A*, *H4C3*, and *H1-0*) appeared to be direct targets of miR-449a and miR-340 (Figure 3E). When looking at the genes downregulated directly and indirectly after miRNA transfection in the bulk RNA-seq, we identified an overall downregulation of glycolysis and chromatin modulators together with effects on p53 signaling (Figure S5C).

In order to assess whether chromatin accessibility would be affected after miRNA transfection, we performed ATAC-seq. Intriguingly, the miRNA-mediated targeting of histone modifications appeared to directly drive FN-RMS identity modulation at the epigenetic level, as seen by increased chromatin accessibility following transfection (Figure 3F). At the single-nucleus level, miRNAs appear to reduce the accessibility of the epigenetic regulator *EZH2* (Figure S6A) as well as the myogenic gene *MYOG* (Figure S6B), with increased accessibility of the muscle-related and tumor suppressor long non-coding RNA *MEG3* (Figure S6C). By looking at the motif enrichment in the snATAC-seq data, a reduced presence of *MYOG* (Figure S6D) and induction of *TP53* (Figure S6E) were observed after miRNA transfection.

We sought to explore whether direct modulation at the epigenetic level combined with proliferation targeting would achieve a similar effect. *EZH2*, *TOP2A*, and *MYBL2* appeared to be completely downregulated after miRNA transfection, together with direct targeting of *MKI67* (Figure S7A). Although there is no current specific inhibitor of *MYBL2*, topotecan has been shown to be a direct inhibitor in neuroblastoma.[16] Thus, by using inhibitors of *EZH2* (tazemetostat), *TOP2A* (doxorubicin), and *MYBL2* (topotecan), we aimed to assess whether we would observe a similar reduction in proliferation and whether these targets need to be downregulated simultaneously to obtain a similar effect. By checking the drugs' effects using a 2,3-bis-(2-methoxy-4-nitro-5-sulfophenyl)-2H-tetrazolium-5-carboxanilide proliferation assay after 96 h, we observed that the use of tazemetostat alone did not have any effects, while the synergy with doxorubicin and topotecan had the most impressive effect in reducing the proliferation of FN-RMS cells (Figure S7B).

As we observed an effect at the metabolic level with downregulation of glycolysis-related genes, we performed metabolomics analysis to comprehensively explore the metabolic alterations associated with FN-RMS following miRNA perturbation. At the intracellular level (Figure 3G), we observed an accumulation of pyruvate and metabolites related to amino acids after miRNA transfection, with higher secretion of alanine in the extracellular environment (Figure S8A). Among the top enriched metabolite-related KEGG pathways, we found increased aminoacyl-tRNA after miRNA transfection (Figure S8B). In line with the human cell line, a similar epigenetic and metabolic shift was also observed in murine FN-RMS after miRNA transfection (Figures S8C–S8D).

Taken together, the identified miRNAs appear to modulate the cell identity at the transcriptomic, epigenomic, and metabolomic level with a shift toward a quiescent state.

Inhibition of MPC recapitulates the effects observed with miRNA perturbation

To elucidate the gene expression distinctions between skeletal muscle and FN-RMS, we focused on the downregulated pathways from the analysis of patients with FN-RMS compared with skeletal muscle. Interestingly, pyruvate and other metabolism-related pathways were among the most significantly downregulated (Figure 4A). After miR-449a+340 transfection, we observed direct and indirect targeting of glycolysis, which, combined with the metabolomic results with an increased

(D and E) Principal-component analysis (D) and volcano plot (E) of upregulated (red) and downregulated (blue) genes in the vehicle- versus miRNA-transfected human FN-RMS cell line RD18 (n = 4).
(F) KEGG pathways involved after miRNA transfection according to bulk RNA-seq.
(G) snRNA-seq of the human FN-RMS cell line after miRNA perturbation compared to vehicle (6,688 cells).
(H) Cell cycle analysis from the snRNA-seq data using the cell cycle-related gene list from Tirosh et al.[11]

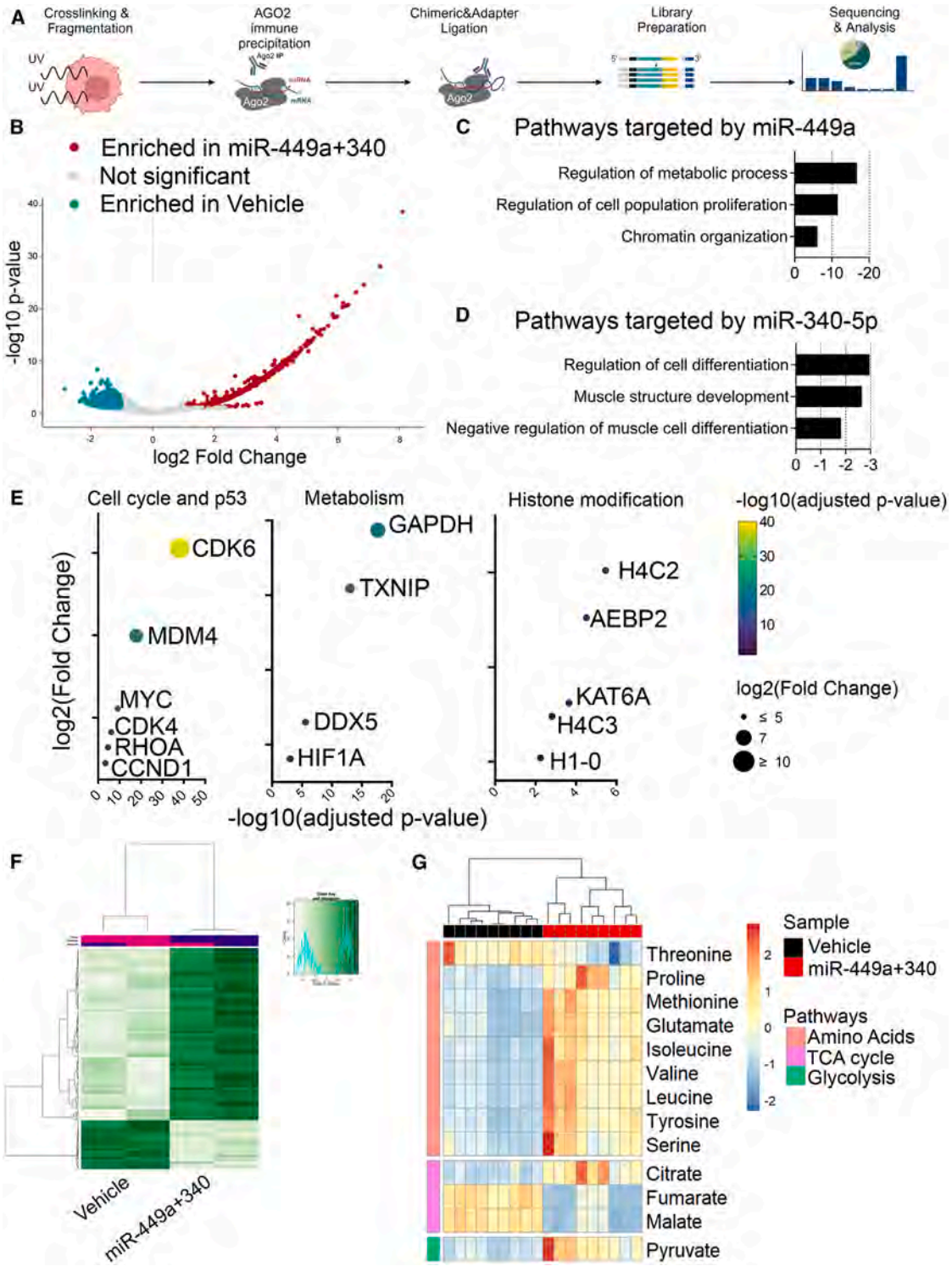

Figure 3. miR-449a+340 directly affect FN-RMS at the epigenetic and metabolic levels

(A) BioRender illustration showing the miR-eCLIP system of immune precipitation to assess direct miRNA targets.
(B) Volcano plot showing the results of differential analysis after eCLIP between vehicle and miR-449a+340 (n = 3).
(C and D) Pathways enriched by the direct targets of (C) miR-449a and (D) miR-340-5p.

(legend continued on next page)

accumulation of pyruvate in the cell, hinted at a key role in the pyruvate uptake of the mitochondria for the observed effects after miRNA transfection. In addition, downregulation of *MPC1* and *MPC2*, encoding for mitochondrial pyruvate carrier (MPC), could be observed in the RNA-seq after transfection (Figure 4B). Thus, we sought to explore whether the modulation of pyruvate entry in the mitochondria would mimic the results obtained with miRNAs. By performing genetic validation, we observed that targeting *MPC2* using small interfering RNAs (siRNAs) similarly obtained an effect on cell cycle exit in FN-RMS (Figure S9A). This hinted at MPC as a required metabolic component of FN-RMS proliferation. Thus, we treated FN-RMS cell line models with the established MPC inhibitor (MPCi) UK5099. By means of proteomics analysis, we observed that lower concentrations (2 and 10 μM) did not sort any effect at the protein level, while 40 μM appeared to skew the treated samples in the principal-component analysis (Figure S9B), as seen also in the volcano plot (Figure 4C). When looking at the pathways involved, we observed downregulation of cell cycle-related proteins and upregulation of amino acids and pyruvate metabolism-related proteins (Figure 4D). Cell cycle exit caused by UK-5099 was further confirmed by means of EdU analysis in both FN-RMS and FP-RMS cell lines (Figure S9C).

In order to address whether MPC modulation would affect mitochondrial respiration, we performed SeaHorse analysis. Here, we observed a reduction in the oxygen consumption rate of human FN-RMS after both miRNA and MPCi perturbation (Figure 4E), affecting both basal respiration (Figure 4F) and maximal respiratory capacity (Figure 4G). While we observed a reduction in proliferation of cells after MPCi or miRNA perturbation (Figure S9D), both miRNAs and MPCi appeared to induce an increase in nucleus size (Figure S9E), but miR-449a+340 increased the percentage of senescent cells (Figure S9F).

Among the shared downregulated genes and proteins after either miRNA or MPCi perturbation, we found MYOG, cell-cycle related TOP2A and MKI67, AURKB, and the histone modifiers H1-1 and H1-6 (Figure S10A). By checking myogenic differentiation by western blot, both MPCi and miRNAs abolished MYOG expression, but myoblast marker myogenic factor 5 (MYF5) expression was upregulated after MPCi (Figure S10B).

Thus, blockade of MPC appears to have a role in cell cycle exit and in the reduction of metabolic activity observed after miRNA transfection of FN-RMS cell models.

MPC inhibition and miRNAs target FN-RMS migration and proliferation in tumor-bearing mice and improve overall exercise capability

We aimed to assess the effects of miRNAs and MPCi *in vivo* using our immune-competent FN-RMS syngeneic murine model.

Following pre-treatment of the murine FN-RMS cell line and its subsequent injection in the femoral artery to replicate the hematogenous spread pattern of this cancer, we observed a similar reduction in proliferation after either miRNA or MPCi perturbation (Figures 5A and 5B).

As a role of pyruvate metabolism blockade in decreasing metastasis has been described previously in other tumor models,[17] we aimed to assess the effects of MPCi and miRNAs on the metastatic potential of the murine FN-RMS model. We first assessed the effects on migration and invasion potential by measuring the protein expression of focal adhesion kinase (FAK) and vascular endothelial cadherin (VE-CAD). Following either MPCi or miRNA treatment, we observed reduced protein expression of both FAK and VE-CAD (Figure S10C). Both *in vivo* (Figures 5C and 5D) and *ex vivo* (Figures 5E and 5F) measurements confirmed the reduction of lung metastasis after miRNA and MPCi treatment in FN-RMS. This effect was also evident at the histological level, where miR-449a+340 and MPCi abolished the presence of visible lung metastasis (Figure 5G). Finally, in order to address skeletal muscle functionality in tumor-bearing mice, we checked the time (Figure S10D), distance covered (Figure S10E), and power output (Figures S10F–S10G; Table S2) with a treadmill exhaustion test. Compared to vehicle, MPCi- and miRNA-treated tumor-bearing mice were able to perform similarly as sham mice.

Taken together, these data show that MPCi and miRNAs similarly reduce the proliferation and metastatic potential of FN-RMS *in vivo*.

DISCUSSION

In this study, we identified two key miRNAs, miR-449a and miR-340, that are significantly downregulated in FN-RMS and play crucial roles in the regulation of the cell cycle and p53 signaling, respectively. These miRNAs were identified through a comprehensive analysis of miRNA expression profiles in patients with FN-RMS, and subsequent pathway analysis highlighted their involvement in the regulation of proliferation in FN-RMS cells.

Transfection of FN-RMS cells with miR-449a induced cell-cycle arrest, shifting cells from S phase to G0/G1 phase, while miR-340 downregulated p53 pathway-related genes. To the best of our knowledge, the effect of these miRNAs has not been studied previously in FN-RMS. In the literature, it has been described how miR-340 may act either as an oncogene or a tumor suppressor by targeting genes related to proliferation, apoptosis, and metastasis.[18] On the other hand, miR-449a appears to target S/G2-phase cyclin in other sarcomas.[19]

We tested miR-449a and miR-340 in a co-culture model of FN-RMS and myogenically differentiating cells. miR-449a effectively blocked FN-RMS cell proliferation but similarly halted myogenic differentiation. However, when combined with miR-340, tumor suppression was enhanced, while skeletal muscle differentiation was preserved. Thus, we decided to perform further experiments using the combination of miRNAs.

After transfection of FN-RMS cell models with miR-449a+340, RNA-seq analysis revealed significant changes in gene expression, particularly in pathways related to the cell cycle and p53 signaling. The most upregulated pathway appeared to be related to cilium organization and cilium assembly; the cilium is an

(E) Selection of direct targets of miR-449a+340.
(F) Heatmap of bulk ATAC-seq analysis of the human FN-RMS cell line after miRNA transfection compared to vehicle ($n = 2$).
(G) Intracellular metabolite accumulation in the human FN-RMS cell line after miRNA transfection. Statistically significant (unpaired t test, $p < 0.05$) metabolites and their log-fold change are shown ($n = 9$).

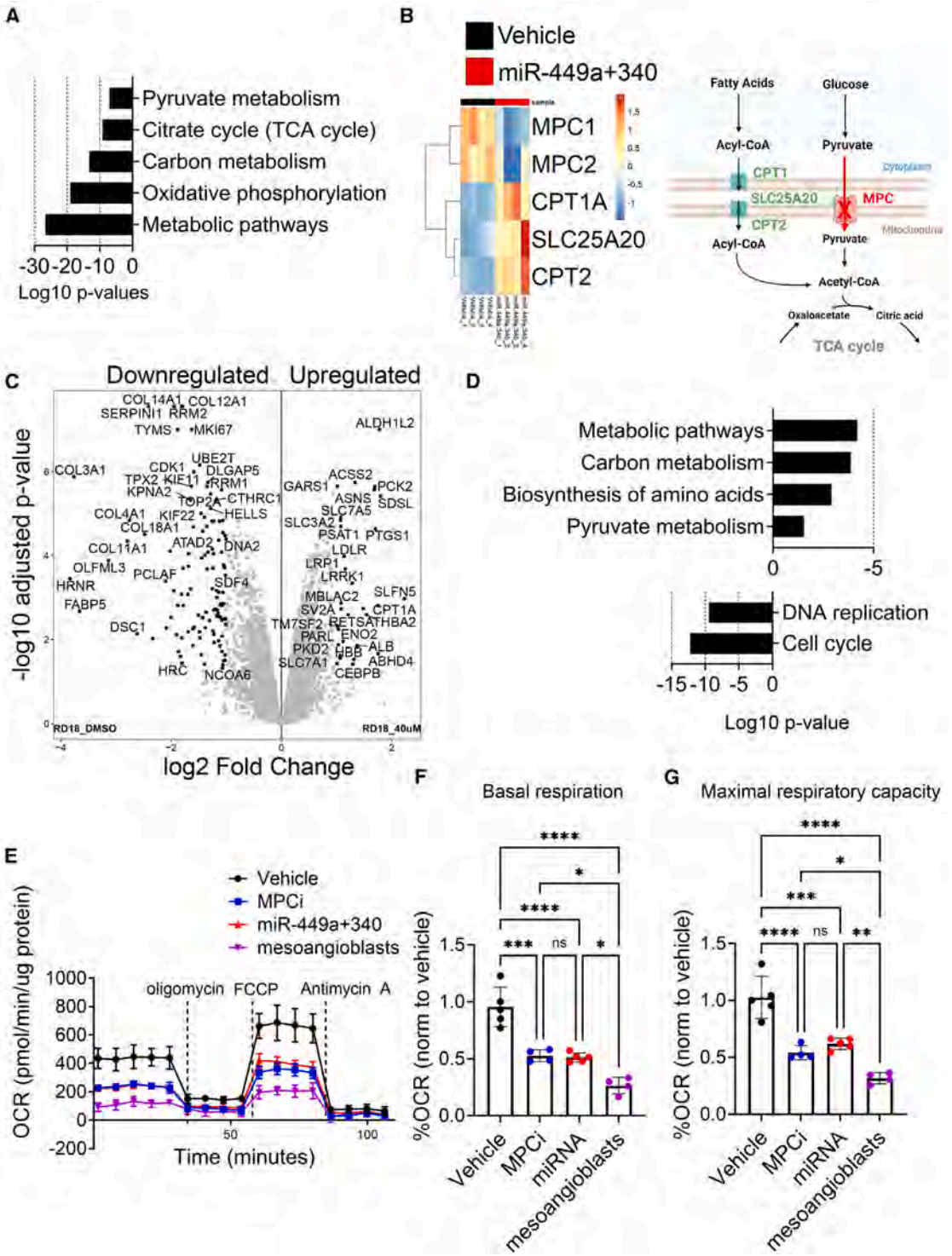

Figure 4. Inhibition of MPC recapitulates the effects observed with miRNA perturbation

(A) Metabolism-related KEGG pathways related to the downregulated genes in the RNA-seq analysis of patients with FN-RMS (GSE108022).

(B) Heatmap of mitochondrial membrane genes shown to be perturbated after miRNA transfection (n = 4) together with a BioRender schematic representation.

(C) Volcano plot of differential analysis of the FN-RMS cell line after MPCi UK-5099 treatment.

(D) Related pathways enriched in up- and downregulated proteins (n = 3).

(legend continued on next page)

antenna-like organelle essential for coordinating extracellular signals that regulate muscle cell growth, development, and homeostasis.[20] Previous research has described the role of cilium formation in restoring differentiation potential in RMS.[21] Similarly, the cilium structure has been described in quiescent muscle stem cells but is disassembled in activated cells.[22] Indeed, previously reported data show that quiescent muscle cells, upon exit from the cell cycle, undergo cilium formation.[20] Cilium formation and the inability of the cell to disassemble has also been linked to the development of premature senescence.[23] The increased expression of genes related to this pathway suggests a shift toward quiescence.

The heterogeneity of FN-RMS has been explored in recent single-cell studies, where distinct subpopulations have been characterized. A study by Danielli et al.[14] builds on previous work by Patel et al.,[24] Wei et al.,[15] and Danielli et al.[25] with the goal of creating a unified nomenclature for the tripartite cell state landscape of FN-RMS. Based on their analysis, a gene signature was generated for progenitor, proliferative, and differentiated states. Conversely, DeMartino et al.[13] similarly identified three distinct cell states—progenitor-like, myoblast-like, and mesenchymal-like—that differ from Danielli et al.'s findings,[14] particularly in the developmental model underlying FN-RMS evolution. According to DeMartino et al., FN-RMS originates from a proliferative progenitor-like state that differentiates into either a myoblast-like or a mesenchymal-like state, with enrichment of genes from these differentiated states correlating with increased survival probability in patients with FN-RMS. The studies on which Danielli et al.'s work is built, however, characterize the mesenchymal-like state (termed progenitor) as a quiescent, cancer stem cell-like state that replenishes the tumor after chemotherapy. Using the gene signatures identified in the aforementioned studies, we found that the progenitor-like/proliferative population signature was completely abolished following miR-449a+340 transfection, with a slight upregulation of genes related to the mesenchymal-like/progenitor state. To further investigate the potential increase in stemness, we performed a tumorsphere formation assay after miR-449a+340 transfection. Indeed, we observed a reduced tumorsphere size, indicating a quiescent mesenchymal state that is differentiated and not contributing to tumor regrowth.

To better understand the direct and indirect effects of miR-449a+340 in FN-RMS, we performed immunoprecipitation analysis (eCLIP) to characterize where the AGO2 complex would form 24 h after transfection. Among the direct targets of miR-449a+340, we identified histone-related gene modifiers such as *H4C2*, *AEBP2*, *KAT6A*, *H4C3*, and *H1-0*. The targeting of histone H1 genes has been shown previously to induce upregulation of interferon-stimulated genes in breast cancer.[26] Indeed, we also observed upregulation of interferon-related genes in our RNA-seq analysis, hinting at a similar DNA damage response caused by H1 downregulation, among other factors. In addition, H1 has been shown to be a critical regulator of gene silencing through localized control of chromatin compaction.[27]

AEBP2, another direct target of miR-449a, interacts with polycomb repressor complex 2 (PRC2) by enhancing the catalytic activity of its histone methylation activity.[28] Indeed, in our RNA-seq analysis 60 h after miR-449a+340 transfection, we found downregulation of the PRC2-related genes *JARID2* and *EZH2*. *EZH2* has been described previously to be upregulated in patients with RMS,[29] and in melanoma, ciliogenesis and cilium-dependent growth inhibition is induced by *EZH2* inhibition.[30] To confirm whether targeting histone methylation activity would result in chromatin opening, we performed ATAC-seq analysis and found an overall increase in chromatin accessibility after miRNA transfection, confirming the downstream effect of miRNAs in inducing hypomethylation.

MYC, *GAPDH*, and *HIF1A* appeared to be direct targets of miR-449a. *MYC* is regarded as one of the key regulators of both cell growth and metabolism the latter via activation of *HIF1A*[31] and *GAPDH*.[32] Since we observed downregulation of glycolysis-related genes but an increased presence of intracellular pyruvate after miR-449a+340 transfection, we hypothesized that the entry of pyruvate into mitochondria was blocked, favoring a shift toward fatty acid metabolism. Intriguingly, during muscle stem cell activation from quiescence to proliferation, a metabolic switch from fatty-acid oxidation to glycolysis has been described.[33] This hints at a need for FN-RMS to switch toward fatty acid metabolism to rewire its phenotype toward a non-tumorigenic one. Indeed, fatty acid metabolism appears among the downregulated pathways in patients with FN-RMS compared to skeletal muscle. This was similarly observed in a previous study of the genetically engineered murine FN-RMS model we used,[6] where the RNA-seq analysis showed downregulation of fatty acid metabolism in murine FN-RMS compared to the control.

We sought to explore the effect of blocking the mitochondrial pyruvate carrier (MPC) to see whether this would mimic the results obtained with miR-449a+340. By performing siRNA experiments, we observed that silencing *MPC2* led to cell cycle exit and a reduction in proliferation. Consequently, we decided to use the MPCi UK-5099, which has been documented extensively in the literature for experiments related to pyruvate entry into mitochondria. We performed proteomics analysis of an FN-RMS cell model exposed to 2, 10, and 40 μM UK-5099 based on the dose-dependent effects described in macrophages, where lower doses achieved similar metabolic modulation.[34] However, we found that a dose of 40 μM was required to achieve a similar cell cycle exit as observed with siRNA. Indeed, in prostate cancer, 50 μM MPC has been shown to activate the G1/S checkpoint, as demonstrated by Cas9 knockout of *MPC1* and *MPC2*.[35] The regulation of MPC has been linked to p53, as upregulation of *BBC3* (also known as *PUMA*) leads to decreased mitochondrial pyruvate uptake.[36] Indeed, after miR-449a+340 transfection, we observed *BBC3* upregulation among the p53-related genes. In addition, murine models of MPC knockout showed increased p53 activity, upregulation of genes related

(E–G) Seahorse measurement of the oxygen consumption rate of the human FN-RMS cell line and (F) percentage change of the oxygen consumption rate at basal respiration and (G) at maximal respiratory capacity after MPCi and miRNAs compared to vehicle, with human skeletal muscle cell (MABs) used as a healthy control ($n = 4$).

Data are presented as mean ± SD, one-way ANOVA. *$p < 0.05$, **$p < 0.01$, ***$p < 0.001$, ****$p < 0.0001$.

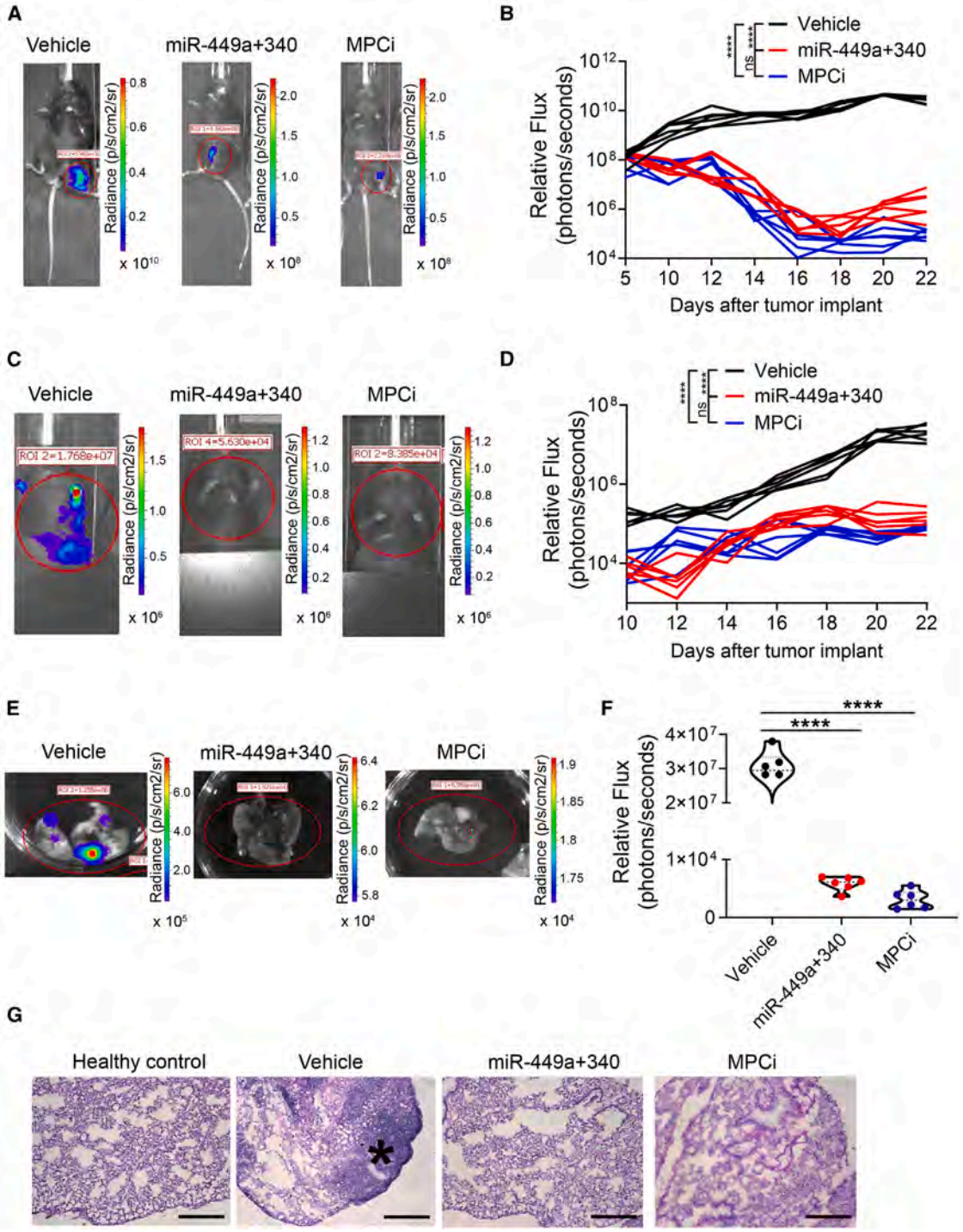

Figure 5. MPCi and miRNAs similarly target migration and proliferation

(A and B) Representative image of the bioluminescent signal *in vivo* on day 22 following the injection of the murine FN-RMS cell line after miRNA or MPCi perturbation compared to vehicle (A) and the relative photon flux (pulse/s) from the regions of interest (ROIs) (B) (n = 6 per group).

(C and D) Representative image of the bioluminescent signal *in vivo* from lungs on day 22 following femoral artery injection of the murine FN-RMS cell line after miRNA or MPCi perturbation compared to vehicle (C) the photon flux from the ROIs (D) (n = 6 per group).

(legend continued on next page)

to the interferon pathway, and decreased expression of *MYC* and *TXNIP*.[37] Intriguingly, *MYC* and *TXNIP* appear to be among the direct targets of miR-449a, with *TXNIP* targeting shown previously in myoblasts to lead to deficient respiration on pyruvate.[38] In skeletal muscle, a high-fat diet is associated with an increase in MPC expression in the liver.[39] Knockdown of MPC increases fatty acid oxidation in C2C12 skeletal muscle cells, as suppression of pyruvate transport induces a form of metabolic flexibility associated with the use of fatty acids and branched-chain amino acid oxidation as catabolic and anabolic fuels.[40] At the proteomic level, it was intriguing to observe a similar upregulation of CPT1 after treatment with the MPCi UK-5099, suggesting increased acyl-coenzyme A uptake in the mitochondria to counteract the lack of pyruvate entry into the citric acid cycle. To the best of our knowledge, our study is the first one investigating the role of MPC in FN-RMS, and the notable decrease in the entry of pyruvate into mitochondria appears to have a direct role in establishing the quiescence program of FN-RMS. Overall, targeting the MPC with inhibitors mimicked the effects of miRNA perturbation, reducing cell cycle progression and metabolic activity.

In our study, we investigated the effects of miRNAs and MPCi in an immune-competent FN-RMS murine model. To mimic the cancer's hematogenous spread, particularly to the lungs, we injected FN-RMS cells into the femoral artery. Following treatment with miRNAs or MPCi, we observed a similar reduction in tumor cell proliferation, indicating that both interventions are effective in inhibiting tumor growth. We also assessed skeletal muscle function in tumor-bearing mice using treadmill tests. Remarkably, mice treated with miRNAs or MPCi performed comparably to healthy controls, suggesting that these treatments can maintain muscle function. Finally, consistent with previous findings linking pyruvate metabolism blockade to reduced metastasis,[17] we observed a significant reduction in lung metastasis by both *in vivo* and *ex vivo* measurements following treatment with miRNAs and MPCi. Histological analysis further confirmed fewer lung metastases in treated mice.

In conclusion, upregulation of miR-449a and miR-340 led to a cell population switch toward quiescence. We provide evidence that the combination of miRNAs is able to reduce cell identity fluctuations observed in FN-RMS, pushing the tumor out of the ''infinite loop'' and locking it into a perpetual undifferentiated stage.

Limitations of the study

In this study, we used pre-treatment of tumor cells before implantation to treat the cells instead of *in vivo* delivery systems. However, the latter was beyond the scope of our study, as we focused on unveiling the mechanisms underlying the overall effects observed in miRNA-treated FN-RMS. We utilized intra-femoral artery injection of FN-RMS cells to mimic the hematogenous spread pattern observed in this cancer, particularly its affinity for lung metastasis. This method, chosen for its clinical relevance, addresses the challenge of limited animal models displaying high frequencies of metastases in RMS research. Indeed, intra-femoral injection has been shown to effectively increase the likelihood of developing metastatic tumors, thereby contributing to a more comprehensive understanding of RMS metastasis biology. Finally, in our metabolic studies, although the analysis hints at the push toward a fatty acid metabolic switch in miRNA-treated FN-RMS cells, we did not investigate the increased production or uptake of fatty acids.

RESOURCE AVAILABILITY

Lead contact

Requests for further information, reagents, and source data should be directed to and will be fulfilled by the lead contact, Maurilio Sampaolesi (maurilio.sampaolesi@kuleuven.be).

Materials availability

This study did not generate new unique reagents.

Data and code availability

- Transcriptomics and ATAC-seq data have been deposited at NCBI GEO and are publicly available as of the date of publication. Accession numbers are listed in the key resources table.
- Proteomics data have been deposited into the ProteomeXchange Consortium via the PRIDE partner repository and are publicly available as of the date of publication. Accession numbers are listed in the key resources table.
- This paper does not report original code.
- Any additional information required to reanalyze the data reported in this work is available from the lead contact upon request.

ACKNOWLEDGMENTS

M.S. acknowledges funding from The Research Foundation Flanders (FWO) (#G058924N), INTERREG – Euregio Meuse-Rhine (GYM, Generate Your Muscle 2020-EMR116), Small Research Infrastructure KU Leuven–BioAssemblyBot 400 (KA/20/088), ERA-NET ERA4Health CARDINNOV: AmnioSMART #G0GE223N, and the Ricerca Finalizzata from the Italian Ministry of Health (RF-2019-12369703). E.P. was supported by FWO (#1S90718N). L.Y. was supported by KU Leuven Rondoufonds voor Duchenne Onderzoek (EQQ-FODUCH-O2010). B.K.v.d.V. was supported by FWO (#11E7920N). K.P.K. acknowledges funding from FWO (#G092518N and #G0C6820N). S.-M.F. acknowledges funding from the European Research Council under ERC Consolidator grant agreement 771486–MetaRegulation, FWO Projects, Beug Foundation, Stichting Tegen Kanker, Fonds Baillet Latour, and KU Leuven. J.T.Y. acknowledges funding from NIH R21 CA234665 and NIH 1R01 CA277686. We would like to thank the group of Frederic Lluis for the scientific discussions and for helping with the EdU analysis. We would also like to thank Jeff DeMartino, Michael Meister, and Jarno Drost for performing the analysis of Figure S3C from their dataset. We want to thank the collaborators from Proteomics Leuven - Laboratory of Applied Mass Spectrometry (LAMaS) for their valuable contribution to the research presented in this paper.

(E and F) Representative image of the bioluminescent signal *ex vivo* from lungs of tumor-bearing murine FN-RMS models after miRNA or MPCi perturbation compared to vehicle (E) and the photon flux from the ROIs (F) ($n = 6$ per group). The p values are also shown in Table S2. Data presented as mean ± SD, one-way ANOVA. *$p < 0.05$, **$p < 0.01$, ***$p < 0.001$, ****$p < 0.0001$; ns, not significant.

(G) Representative image of hematoxylin and eosin staining of lung sections from healthy control and vehicle-, miRNA-, and MPCi-treated mice. Scale bar: 200 μm.

AUTHOR CONTRIBUTIONS

Conceptualization, E.P. and M.S.; methodology, E.P. and M.S.; investigation, E.P., L.Y., N.G., C.-c.W., G.M.G., E.D., V.M., G.R., B.K.v.d.V., G.S., G.E., and M.P.; resources, A.F., K.P.K., P.C., J.T.Y., and S.-M.F.; writing – original draft, E.P., L.Y., N.G., and M.S.; writing – review & editing, E.P., L.Y., and M.S.; funding acquisition, M.S.; supervision, A.F., K.P.K., P.C., J.T.Y., S.-M.F., A.U., and M.S.

DECLARATION OF INTERESTS

S.-M.F. has received funding from Bayer AG, Merck, Black Belt Therapeutics, Gilead, and Alesta Therapeutics; has consulted for Fund+; and is on the advisory board of Alesta Therapeutics. E.P. and M.S. hold a patent on the use of miRs for the treatment or prevention of rhabdomyosarcoma.

STAR★METHODS

Detailed methods are provided in the online version of this paper and include the following:

- KEY RESOURCES TABLE
- EXPERIMENTAL MODEL AND STUDY PARTICIPANT DETAILS
  - Cell lines and culture conditions
  - *In vivo* experiments
  - Sample size
  - Experimental group allocation
- METHOD DETAILS
  - miRNA/MPCi/siRNA treatment
  - EdU assay
  - RNA isolation and quantitative RT-PCR
  - Co-cultures
  - Immunofluorescence
  - RNA-sequencing (RNA-seq)
  - Multiome snRNA-seq/ATAC-seq using chromium 10x genomics platform
  - Tumorsphere assay
  - miR-eCLIP
  - ATAC-sequencing (ATAC-seq)
  - Drug screening
  - Metabolite extraction and measurements
  - Proteomics
  - Oxygen consumption rate
  - Senescence assay
  - Western blot
  - Reporter cell line
  - Bioluminescence imaging and treadmill exhaustion test
  - Hematoxylin and eosin
- QUANTIFICATION AND STATISTICAL ANALYSIS

SUPPLEMENTAL INFORMATION

Supplemental information can be found online at https://doi.org/10.1016/j.celrep.2024.115171.

Received: January 22, 2024
Revised: September 15, 2024
Accepted: December 17, 2024

REFERENCES

1. Perez, E.A., Kassira, N., Cheung, M.C., Koniaris, L.G., Neville, H.L., and Sola, J.E. (2011). Rhabdomyosarcoma in Children: A SEER Population Based Study. J. Surg. Res. *170*, e243–e251. https://doi.org/10.1016/j.jss.2011.03.001.
2. Quattrocelli, M., and Sampaolesi, M. (2015). The mesmiRizing complexity of microRNAs for striated muscle tissue engineering. Adv. Drug Deliv. Rev. *88*, 37–52. https://doi.org/10.1016/j.addr.2015.04.011.
3. Rotini, A., Martínez-Sarrà, E., Pozzo, E., and Sampaolesi, M. (2018). Interactions between microRNAs and long non-coding RNAs in cardiac development and repair. Pharmacol. Res. *127*, 58–66. https://doi.org/10.1016/j.phrs.2017.05.029.
4. Pozzo, E., Giarratana, N., Sassi, G., Elmastas, M., Killian, T., Wang, C.-C., Marini, V., Ronzoni, F., Yustein, J., Uyttebroeck, A., and Sampaolesi, M. (2021). Upregulation of miR181a/miR212 Improves Myogenic Commitment in Murine Fusion-Negative Rhabdomyosarcoma. Front. Physiol. *12*, 701354. https://doi.org/10.3389/fphys.2021.701354.
5. Giacomazzi, G., Holvoet, B., Trenson, S., Caluwé, E., Kravic, B., Grosemans, H., Cortés-Calabuig, Á., Deroose, C.M., Huylebroeck, D., Hashemolhosseini, S., et al. (2017). MicroRNAs promote skeletal muscle differentiation of mesodermal iPSC-derived progenitors. Nat. Commun. *8*, 1249. https://doi.org/10.1038/s41467-017-01359-w.
6. Nakahata, K., Simons, B.W., Pozzo, E., Shuck, R., Kurenbekova, L., Prudowsky, Z., Dholakia, K., Coarfa, C., Patel, T.D., Donehower, L.A., and Yustein, J.T. (2022). K-Ras and p53 mouse model with molecular characteristics of human rhabdomyosarcoma and translational applications. Dis. Model. Mech. *15*, dmm049004. https://doi.org/10.1242/dmm.049004.
7. Bersani, F., Lingua, M.F., Morena, D., Foglizzo, V., Miretti, S., Lanzetti, L., Carrà, G., Morotti, A., Ala, U., Provero, P., et al. (2016). Deep Sequencing Reveals a Novel miR-22 Regulatory Network with Therapeutic Potential in Rhabdomyosarcoma. Cancer Res. *76*, 6095–6106. https://doi.org/10.1158/0008-5472.CAN-16-0709.
8. Vlachos, I.S., Zagganas, K., Paraskevopoulou, M.D., Georgakilas, G., Karagkouni, D., Vergoulis, T., Dalamagas, T., and Hatzigeorgiou, A.G. (2015). DIANA-miRPath v3.0: deciphering microRNA function with experimental support. Nucleic Acids Res. *43*, W460–W466. https://doi.org/10.1093/nar/gkv403.
9. Hayes, M.N., McCarthy, K., Jin, A., Oliveira, M.L., Iyer, S., Garcia, S.P., Sindiri, S., Gryder, B., Motala, Z., Nielsen, G.P., et al. (2018). Vangl2/RhoA Signaling Pathway Regulates Stem Cell Self-Renewal Programs and Growth in Rhabdomyosarcoma. Cell Stem Cell *22*, 414–427.e6. https://doi.org/10.1016/j.stem.2018.02.002.
10. Kehl, T., Kern, F., Backes, C., Fehlmann, T., Stöckel, D., Meese, E., Lenhof, H.-P., and Keller, A. (2020). miRPathDB 2.0: a novel release of the miRNA Pathway Dictionary Database. Nucleic Acids Res. *48*, D142–D147. https://doi.org/10.1093/nar/gkz1022.
11. Tirosh, I., Izar, B., Prakadan, S.M., Wadsworth, M.H., 2nd, Treacy, D., Trombetta, J.J., Rotem, A., Rodman, C., Lian, C., Murphy, G., et al. (2016). Dissecting the multicellular ecosystem of metastatic melanoma by single-cell RNA-seq. Science *352*, 189–196. https://doi.org/10.1126/science.aad0501.
12. van Dam, T.J.P., Kennedy, J., van der Lee, R., de Vrieze, E., Wunderlich, K.A., Rix, S., Dougherty, G.W., Lambacher, N.J., Li, C., Jensen, V.L., et al. (2019). CiliaCarta: An integrated and validated compendium of ciliary genes. PLoS One *14*, e0216705. https://doi.org/10.1371/journal.pone.0216705.
13. DeMartino, J., Meister, M.T., Visser, L.L., Brok, M., Groot Koerkamp, M.J.A., Wezenaar, A.K.L., Hiemcke-Jiwa, L.S., de Souza, T., Merks, J.H.M., Rios, A.C., et al. (2023). Single-cell transcriptomics reveals immune suppression and cell states predictive of patient outcomes in rhabdomyosarcoma. Nat. Commun. *14*, 3074. https://doi.org/10.1038/s41467-023-38886-8.
14. Danielli, S.G., Wei, Y., Dyer, M.A., Stewart, E., Sheppard, H., Wachtel, M., Schäfer, B.W., Patel, A.G., and Langenau, D.M. (2024). Single cell transcriptomic profiling identifies tumor-acquired and therapy-resistant cell states in pediatric rhabdomyosarcoma. Nat. Commun. *15*, 6307. https://doi.org/10.1038/s41467-024-50527-2.
15. Wei, Y., Qin, Q., Yan, C., Hayes, M.N., Garcia, S.P., Xi, H., Do, D., Jin, A.H., Eng, T.C., McCarthy, K.M., et al. (2022). Single-cell analysis and functional

characterization uncover the stem cell hierarchies and developmental origins of rhabdomyosarcoma. Nat. Can. (Ott.) *3*, 961–975. https://doi.org/10.1038/s43018-022-00414-w.

16. Sottile, F., Gnemmi, I., Cantilena, S., D'Acunto, W.C., and Sala, A. (2012). A chemical screen identifies the chemotherapeutic drug topotecan as a specific inhibitor of the B-MYB/MYCN axis in neuroblastoma. Oncotarget *3*, 535–545. https://doi.org/10.18632/oncotarget.498.
17. Elia, I., Rossi, M., Stegen, S., Broekaert, D., Doglioni, G., van Gorsel, M., Boon, R., Escalona-Noguero, C., Torrekens, S., Verfaillie, C., et al. (2019). Breast cancer cells rely on environmental pyruvate to shape the metastatic niche. Nature *568*, 117–121. https://doi.org/10.1038/s41586-019-0977-x.
18. Bassot, A., Dragic, H., Haddad, S.A., Moindrot, L., Odouard, S., Corlazzoli, F., Marinari, E., Bomane, A., Brassens, A., Marteyn, A., et al. (2023). Identification of a miRNA multi-targeting therapeutic strategy in glioblastoma. Cell Death Dis. *14*, 630. https://doi.org/10.1038/s41419-023-06117-z.
19. Shekhar, R., Priyanka, P., Kumar, P., Ghosh, T., Khan, M.M., Nagarajan, P., and Saxena, S. (2019). The microRNAs miR-449a and miR-424 suppress osteosarcoma by targeting cyclin A2 expression. J. Biol. Chem. *294*, 4381–4400. https://doi.org/10.1074/jbc.RA118.005778.
20. Wang, L., and Dynlacht, B.D. (2018). The regulation of cilium assembly and disassembly in development and disease. Dev. Camb. Engl. *145*, dev151407. https://doi.org/10.1242/dev.151407.
21. Fu, W., Asp, P., Canter, B., and Dynlacht, B.D. (2014). Primary cilia control hedgehog signaling during muscle differentiation and are deregulated in rhabdomyosarcoma. Proc. Natl. Acad. Sci. USA *111*, 9151–9156. https://doi.org/10.1073/pnas.1323265111.
22. Jaafar Marican, N.H., Cruz-Migoni, S.B., and Borycki, A.-G. (2016). Asymmetric Distribution of Primary Cilia Allocates Satellite Cells for Self-Renewal. Stem Cell Rep. *6*, 798–805. https://doi.org/10.1016/j.stemcr.2016.04.004.
23. Jeffries, E.P., Di Filippo, M., and Galbiati, F. (2019). Failure to reabsorb the primary cilium induces cellular senescence. FASEB J. Off. Publ. Fed. Am. Soc. Exp. Biol. *33*, 4866–4882. https://doi.org/10.1096/fj.201801382R.
24. Patel, A.G., Chen, X., Huang, X., Clay, M.R., Komorova, N., Krasin, M.J., Pappo, A., Tillman, H., Orr, B.A., McEvoy, J., et al. (2022). The myogenesis program drives clonal selection and drug resistance in rhabdomyosarcoma. Dev. Cell *57*, 1226–1240.e8. https://doi.org/10.1016/j.devcel.2022.04.003.
25. Danielli, S.G., Porpiglia, E., De Micheli, A.J., Navarro, N., Zellinger, M.J., Bechtold, I., Kisele, S., Volken, L., Marques, J.G., Kasper, S., et al. (2023). Single-cell profiling of alveolar rhabdomyosarcoma reveals RAS pathway inhibitors as cell-fate hijackers with therapeutic relevance. Sci. Adv. *9*, eade9238. https://doi.org/10.1126/sciadv.ade9238.
26. Izquierdo-Bouldstridge, A., Bustillos, A., Bonet-Costa, C., Aribau-Miralbés, P., García-Gomis, D., Dabad, M., Esteve-Codina, A., Pascual-Reguant, L., Peiró, S., Esteller, M., et al. (2017). Histone H1 depletion triggers an interferon response in cancer cells via activation of heterochromatic repeats. Nucleic Acids Res. *45*, 11622–11642. https://doi.org/10.1093/nar/gkx746.
27. Willcockson, M.A., Healton, S.E., Weiss, C.N., Bartholdy, B.A., Botbol, Y., Mishra, L.N., Sidhwani, D.S., Wilson, T.J., Pinto, H.B., Maron, M.I., et al. (2021). H1 histones control the epigenetic landscape by local chromatin compaction. Nature *589*, 293–298. https://doi.org/10.1038/s41586-020-3032-z.
28. Cao, R., and Zhang, Y. (2004). SUZ12 Is Required for Both the Histone Methyltransferase Activity and the Silencing Function of the EED-EZH2 Complex. Mol. Cell *15*, 57–67. https://doi.org/10.1016/j.molcel.2004.06.020.
29. Ciarapica, R., Carcarino, E., Adesso, L., De Salvo, M., Bracaglia, G., Leoncini, P.P., Dall'agnese, A., Verginelli, F., Milano, G.M., Boldrini, R., et al. (2014). Pharmacological inhibition of EZH2 as a promising differentiation therapy in embryonal RMS. BMC Cancer *14*, 139. https://doi.org/10.1186/1471-2407-14-139.
30. Zingg, D., Debbache, J., Peña-Hernández, R., Antunes, A.T., Schaefer, S.M., Cheng, P.F., Zimmerli, D., Haeusel, J., Calçada, R.R., Tuncer, E., et al. (2018). EZH2-Mediated Primary Cilium Deconstruction Drives Metastatic Melanoma Formation. Cancer Cell *34*, 69–84.e14. https://doi.org/10.1016/j.ccell.2018.06.001.
31. Doe, M.R., Ascano, J.M., Kaur, M., and Cole, M.D. (2012). Myc posttranscriptionally induces HIF1 protein and target gene expression in normal and cancer cells. Cancer Res. *72*, 949–957. https://doi.org/10.1158/0008-5472.CAN-11-2371.
32. Osthus, R.C., Shim, H., Kim, S., Li, Q., Reddy, R., Mukherjee, M., Xu, Y., Wonsey, D., Lee, L.A., and Dang, C.V. (2000). Deregulation of Glucose Transporter 1 and Glycolytic Gene Expression by c-Myc. J. Biol. Chem. *275*, 21797–21800. https://doi.org/10.1074/jbc.c000023200.
33. Ryall, J.G., Cliff, T., Dalton, S., and Sartorelli, V. (2015). Metabolic Reprogramming of Stem Cell Epigenetics. Cell Stem Cell *17*, 651–662. https://doi.org/10.1016/j.stem.2015.11.012.
34. Ran, L., Zhang, S., Wang, G., Zhao, P., Sun, J., Zhou, J., Gan, H., Jeon, R., Li, Q., Herrmann, J., and Wang, F. (2023). Mitochondrial pyruvate carrier-mediated metabolism is dispensable for the classical activation of macrophages. Nat. Metab. *5*, 804–820. https://doi.org/10.1038/s42255-023-00800-3.
35. Bader, D.A., Hartig, S.M., Putluri, V., Foley, C., Hamilton, M.P., Smith, E.A., Saha, P.K., Panigrahi, A., Walker, C., Zong, L., et al. (2019). Mitochondrial pyruvate import is a metabolic vulnerability in androgen receptor-driven prostate cancer. Nat. Metab. *1*, 70–85. https://doi.org/10.1038/s42255-018-0002-y.
36. Kim, J., Yu, L., Chen, W., Xu, Y., Wu, M., Todorova, D., Tang, Q., Feng, B., Jiang, L., He, J., et al. (2019). Wild-Type p53 Promotes Cancer Metabolic Switch by Inducing PUMA-Dependent Suppression of Oxidative Phosphorylation. Cancer Cell *35*, 191–203.e8. https://doi.org/10.1016/j.ccell.2018.12.012.
37. Ramstead, A.G., Wallace, J.A., Lee, S.-H., Bauer, K.M., Tang, W.W., Ekiz, H.A., Lane, T.E., Cluntun, A.A., Bettini, M.L., Round, J.L., et al. (2020). Mitochondrial Pyruvate Carrier 1 Promotes Peripheral T Cell Homeostasis through Metabolic Regulation of Thymic Development. Cell Rep. *30*, 2889–2899.e6. https://doi.org/10.1016/j.celrep.2020.02.042.
38. Katsu-Jiménez, Y., Vázquez-Calvo, C., Maffezzini, C., Halldin, M., Peng, X., Freyer, C., Wredenberg, A., Giménez-Cassina, A., Wedell, A., and Arnér, E.S.J. (2019). Absence of TXNIP in Humans Leads to Lactic Acidosis and Low Serum Methionine Linked to Deficient Respiration on Pyruvate. Diabetes *68*, 709–723. https://doi.org/10.2337/db18-0557.
39. Yu, J., Laybutt, D.R., Youngson, N.A., and Morris, M.J. (2022). Concurrent betaine administration enhances exercise-induced improvements to glucose handling in obese mice. Nutr. Metabol. Cardiovasc. Dis. *32*, 2439–2449. https://doi.org/10.1016/j.numecd.2022.08.012.
40. Vacanti, N.M., Divakaruni, A.S., Green, C.R., Parker, S.J., Henry, R.R., Ciaraldi, T.P., Murphy, A.N., and Metallo, C.M. (2014). Regulation of substrate utilization by the mitochondrial pyruvate carrier. Mol. Cell *56*, 425–435. https://doi.org/10.1016/j.molcel.2014.09.024.
41. Love, M.I., Huber, W., and Anders, S. (2014). Moderated estimation of fold change and dispersion for RNA-seq data with DESeq2. Genome Biol. *15*, 550. https://doi.org/10.1186/s13059-014-0550-8.
42. Raudvere, U., Kolberg, L., Kuzmin, I., Arak, T., Adler, P., Peterson, H., and Vilo, J. (2019). g:Profiler: a web server for functional enrichment analysis and conversions of gene lists (2019 update). Nucleic Acids Res. *47*, W191–W198. https://doi.org/10.1093/nar/gkz369.
43. Meister, M.T., Groot Koerkamp, M.J.A., de Souza, T., Breunis, W.B., Frazer-Mendelewska, E., Brok, M., DeMartino, J., Manders, F., Calandrini, C., Kerstens, H.H.D., et al. (2022). Mesenchymal tumor organoid models recapitulate rhabdomyosarcoma subtypes. EMBO Mol. Med. *14*, e16001. https://doi.org/10.15252/emmm.202216001.
44. Marini, V., Marino, F., Aliberti, F., Giarratana, N., Pozzo, E., Duelen, R., Cortés Calabuig, Á., La Rovere, R., Vervliet, T., Torella, D., et al. (2022). Long-term culture of patient-derived cardiac organoids recapitulated

Duchenne muscular dystrophy cardiomyopathy and disease progression. Front. Cell Dev. Biol. *10*, 878311. https://doi.org/10.3389/fcell.2022.878311.

45. Brunton, H., Garner, I.M., Bailey, U.-M., Upstill-Goddard, R., and Bailey, P.J. (2020). Using Chromatin Accessibility to Delineate Therapeutic Subtypes in Pancreatic Cancer Patient-Derived Cell Lines. STAR Protoc. *1*, 100079. https://doi.org/10.1016/j.xpro.2020.100079.

46. Rinaldi, G., Pranzini, E., Van Elsen, J., Broekaert, D., Funk, C.M., Planque, M., Doglioni, G., Altea-Manzano, P., Rossi, M., Geldhof, V., et al. (2021). In Vivo Evidence for Serine Biosynthesis-Defined Sensitivity of Lung Metastasis, but Not of Primary Breast Tumors, to mTORC1 Inhibition. Mol. Cell *81*, 386–397.e7. https://doi.org/10.1016/j.molcel.2020.11.027.

47. Lorendeau, D., Rinaldi, G., Boon, R., Spincemaille, P., Metzger, K., Jäger, C., Christen, S., Dong, X., Kuenen, S., Voordeckers, K., et al. (2017). Dual loss of succinate dehydrogenase (SDH) and complex I activity is necessary to recapitulate the metabolic phenotype of SDH mutant tumors. Metab. Eng. *43*, 187–197. https://doi.org/10.1016/j.ymben.2016.11.005.

48. Demichev, V., Messner, C.B., Vernardis, S.I., Lilley, K.S., and Ralser, M. (2020). DIA-NN: neural networks and interference correction enable deep proteome coverage in high throughput. Nat. Methods *17*, 41–44. https://doi.org/10.1038/s41592-019-0638-x.

49. Perez-Riverol, Y., Bai, J., Bandla, C., García-Seisdedos, D., Hewapathirana, S., Kamatchinathan, S., Kundu, D.J., Prakash, A., Frericks-Zipper, A., Eisenacher, M., et al. (2022). The PRIDE database resources in 2022: a hub for mass spectrometry-based proteomics evidences. Nucleic Acids Res. *50*, D543–D552. https://doi.org/10.1093/nar/gkab1038.

50. Breuls, N., Giarratana, N., Yedigaryan, L., Garrido, G.M., Carai, P., Heymans, S., Ranga, A., Deroose, C., and Sampaolesi, M. (2021). Valproic acid stimulates myogenesis in pluripotent stem cell-derived mesodermal progenitors in a NOTCH-dependent manner. Cell Death Dis. *12*, 677. https://doi.org/10.1038/s41419-021-03936-w.

51. Giarratana, N., Conti, F., La Rovere, R., Gijsbers, R., Carai, P., Duelen, R., Vervliet, T., Bultynck, G., Ronzoni, F., Piciotti, R., et al. (2020). MICAL2 is essential for myogenic lineage commitment. Cell Death Dis. *11*, 654. https://doi.org/10.1038/s41419-020-02886-z.

52. Martínez-Sarrà, E., Montori, S., Gil-Recio, C., Núñez-Toldrà, R., Costamagna, D., Rotini, A., Atari, M., Luttun, A., and Sampaolesi, M. (2017). Human dental pulp pluripotent-like stem cells promote wound healing and muscle regeneration. Stem Cell Res. Ther. *8*, 175. https://doi.org/10.1186/s13287-017-0621-3.

STAR★METHODS

KEY RESOURCES TABLE

REAGENT or RESOURCE	SOURCE	IDENTIFIER
Antibodies		
Myf-5	Santa Cruz Biotechnology	Cat# sc-302, C-20; RRID:AB_631994
MYOG	Hybridoma (in-house)	N/A
FAK	Sigma-Aldrich	Cat # 06–543, D-1; RRID:AB_11214316
phospho-Focal Adhesion Kinase (Tyr397) Antibody	Sigma-Aldrich	Cat # 05–1140, clone 18; RRID:AB_10615489
VE-Cadherin	R&D Systems	Cat # AF-1002, F-8; RRID:AB_2077789
GAPDH	Sigma-Aldrich	Cat #G9545, 0411; RRID:AB_796208
α-Tubulin	Sigma-Aldrich	Cat #T5168, DM1A: RRID:AB_477579
Goat Anti-Mouse IgG (H + L)-HRP Conjugate	Bio-Rad Laboratories	Cat # 1706516; RRID:AB_2921252
Goat Anti-Rabbit IgG (H + L)-HRP Conjugate	Bio-Rad Laboratories	Cat # 1706515; RRID:AB_11125142
Rabbit Anti-Goat IgG (H + L)-HRP Conjugate	Bio-Rad Laboratories	Cat # 1721034; RRID:AB_2617114
Chemicals, peptides, and recombinant proteins		
UK-5099 (MPC inhibitor)	Sigma-Aldrich	Cat # PZ0160
EPZ-6438 (Tazemetostat)	MedChemExpress	Cat # HY-13803
Topotecan	MedChemExpress	Cat # HY-13768
Doxorubicin	Sigma-Aldrich	Cat #D1515
XTT (2,3-Bis-(2-Methoxy-4-Nitro-5-Sulfophenyl)-2H-Tetrazolium-5-Carboxanilide)	Thermo Fisher Scientific	Cat #X6493
Phalloidin solution	Sigma-Aldrich	Cat #P1951
Hoechst 33258 solution	Sigma-Aldrich	Cat # 94403
Critical commercial assays		
Chromium Next GEM Single Cell Multiome ATAC + Gene Expression	10x Genomics	Cat # PN-1000283
SuperScript™ III First-Strand Synthesis SuperMix for qRT-PCR	Thermo Fisher Scientific	Cat # 11752050
Platinum™ SYBR™ Green qPCR SuperMix-UDG	Thermo Fisher Scientific	Cat # 11733046
Purelink® RNA mini kit	Thermo Fisher Scientific	Cat # 12183025
Turbo™ DNA-free kit	Thermo Fisher Scientific	Cat # AM1907
miRCURY LNA miRNA PCR Starter Kit	Qiagen	Cat # 339320
Click-iT™ EdU Cell Proliferation Kit for Imaging, Alexa Fluor™ 647 dye	Thermo Fisher Scientific	Cat #C10340
Seahorse XF Cell Mito Stress Test Kit	Agilent Technologies	Cat # 103015-100
Deposited data		
Raw and analyzed data	This paper	GEO: GSE276201 PRIDE: PXD058278
RNA-seq of FN-RMS patients compared with skeletal muscle	Hayes et al.[9]	GEO: GSE108022
Experimental models: Cell lines		
Human: RD/18	Laboratory of Alessandro Fanzani	RRID:CVCL_IU87
Human: Rh41	Texas Tech University Health Sciences Center-Children's Oncology Group	RRID:CVCL_2176
Human: Rh30	Texas Tech University Health Sciences Center-Children's Oncology Group	RRID:CVCL_0041
Human: RMS012	Laboratory of Frank C.P. Holstege	N/A

(*Continued on next page*)

Continued		
REAGENT or RESOURCE	SOURCE	IDENTIFIER
Human: RMS044	Laboratory of Frank C.P. Holstege	N/A
Human: mesoangioblasts	This paper	N/A
Mouse: KMR46: MyoD-Cre-p53$^{F/+}$/K-Ras^{G12D}	Laboratory of Jason Yustein	N/A
Experimental models: Organisms/strains		
Mouse: C57BL/6J	The Jackson Laboratory	RRID:IMSR_JAX:000664
Oligonucleotides		
miRNA hsa-miR-449a: UGGCAGUGUAUUGUUAGCUGGU	Thermo Fisher Scientific	Assay ID: MC11127
miRNA hsa-miR-340-5p: UUAUAAAGCAAUGAGACUGAUU	Thermo Fisher Scientific	Assay ID: MC12670
siRNA MPC2	Thermo Fisher Scientific	siRNA ID: 22910
Primers for qRT-PCR, see Table S1	This paper	N/A
Recombinant DNA		
Plasmid: EF1a-eGFP-P2A-fLuc	Pozzo et al.[4]	N/A
Software and algorithms		
GraphPad Prism	GraphPad Software	v10.3.0
ImageJ	https://doi.org/10.1038/nmeth.2089	https://imagej.nih.gov/ij/
FlowJo	BD Biosciences	v10.10
Image-Pro Plus	Nikon	v6.0
DESeq2	Love et al.[41]	https://github.com/thelovelab/DESeq2
g:Profiler	Raudvere et al.[42]	https://biit.cs.ut.ee/gprofiler/gost
Seahorse Wave Desktop	Agilent Technologies	v2.6

EXPERIMENTAL MODEL AND STUDY PARTICIPANT DETAILS

Cell lines and culture conditions

The use of human samples for experimental purposes and protocols in the present study was approved by the Ethics Committee and members of the Biobank Board of the University Hospitals Leuven (S68370). For the FN-RMS cell lines, human RD18 cell line was gifted by dr Alessandro Fanzani (University of Brescia, Italy), while murine KMR46 was obtained via materials transfer agreement (MTA) with dr Jason Yustein (Baylor College of Medicine, Houston, TX, USA). For the FP-RMS cell lines, human RH41 and RH30 were received from Texas Tech University Health Sciences Center-Children's Oncology Group in 2017. All cell lines have been regularly tested at arrival and during passages to confirm the absence of Mycoplasma. Cells have not been authenticated.

Human and murine FN-RMS cell lines were cultured in high glucose Dulbecco's Modified Eagles Medium (DMEM-HG) supplemented with 10% fetal bovine serum (FBS) and 1% Penicillin/Streptomycin (P/S). FP-RMS cells were cultured in Iscove's Modified Dulbecco's Medium plus the following supplements (to a final concentration): 20% FBS, 4mM L-Glutamine, 1X ITS (5 μg/mL insulin, 5 μg/mL transferrin, 5 ng/mL selenous acid). Cells were maintained under standard incubator conditions, in a humidified atmosphere (95% air, 5% CO2, normoxia, 37°C) and passaged twice weekly with 0.25% Trypsin-EDTA. All components were purchased from Gibco, Thermo Fisher Scientific (WA, USA).

Human RMS tumoroid cell lines (RMS012 and RMS044) were obtained from Prof. Frank C.P Holstege (UMC Utrecht and Utrecht University, Utrecht, The Netherlands). Tumoroids were cultured as described by Meister et al.[43] Briefly, for cell attachment, culture medium was supplemented with 0.1–0.5% badent membrane extract type 2 (Cultrex Reduced Growth Factor Basement Membrane Extract, type 2, Pathclear, 3533-005-02, R&D Systems, MN, USA). Cells were cultured in complete culture medium (BM1), which is the base medium with the addition of specific components. Cells were passaged at a confluency of 70%–80% using TrypLE Express Enzyme (Gibco, Thermo Fisher Scientific). Cells were maintained under conventional cell culture conditions as described previously.

In vivo experiments

Housing and experimental animal procedures were approved by the Institutional Animal Care and Research Advisory Committee of KU Leuven (ECD #P089/2018). A total of 24 C57Bl/6 mice were used (6 mice per group), Mice were injected between 5 and 6 weeks of age with saline solution (healthy), 5 × 10^5 KMR46 Fluc+ cells (untreated group) or 5 × 10^5 KMR46 Fluc+ cells pretreated for 3 days with miR-449a+340 or MPCi (treated group) resuspended in 50 μL saline water.

Sample size

Sample size for *in vivo* experiments was calculated by means of Sample Size Calculator (parameters: power, 0.80; alpha, 0.05) (G*Power, Heinrich Heine University Düsseldorf, v3.1.9.7). When applicable, sample size analysis was based on average values obtained from preliminary optimization/validation trials.

Experimental group allocation

Mice were equally divided in the experimental groups between male and female. Results did not show an influence or association of sex, gender, or both.

METHOD DETAILS

miRNA/MPCi/siRNA treatment

Before transfection, cells were seeded at 12–15.000 or 50.000 cells in 24- or 6-well plates (Costar, Corning, NY, USA), respectively. One day after plating, cells were transfected using 3 μL/mL of Lipofectamine 2000 and 1.6 μL/mL of either miRNAs or siRNAs at 10 μM concentration, resuspended in Opti-MEM medium (Gibco, Thermo Fisher Scientific). To evaluate transfection efficiency of the protocol, we used FAM3 Dye-Labeled Pre-miR Negative Control (Invitrogen, Thermo Fisher Scientific, #AM17121) 24 h after transfection.

For miRNA treatment, we used mirVana miRNA mimics hsa-miR-449a-5p/-340-5p (Thermo Fisher Scientific, #MC11127 and #MC12670). For siRNA experiments, we used Silencer Pre-designed siRNA targeting human *MPC2* (Ambion, Thermo Fisher Scientific, #AM16708).

For MPC inhibitor (MPCi) treatment, cells were treated with 8 μL (at a final concentration of 40 μM) of UK-5099 (Sigma-Aldrich) previously resuspended in dimethyl sulfoxide (DMSO) (Sigma-Aldrich), in 2 mL of Opti-MEM medium. For the control group, cells were treated with 8 μL of DMSO in 2 mL of Opti-MEM medium. After 60–65 h of transfection, cells were trypsinized, counted and either frozen or employed for subsequent experiments.

EdU assay

5-ethynyl-2 deoxyuridine (EdU) staining was performed using the Click-iT EdU Cell Proliferation Kit for Imaging, Alexa Fluor 647 dye from Invitrogen, Thermo Fisher Scientific, according to the manufacturers' advice. Briefly, after EdU incubation of 1-2h, cell pellets were fixed with 4% paraformaldehyde (PFA) (Sigma-Aldrich), permeabilized with 0.5% Triton X-100 in phosphate buffered saline (PBS) (Gibco, Thermo Fisher Scientific) for 20 min and subsequently treated with Click-iTreaction cocktail at room temperature for 10 min. Afterward, cells were washed and incubated in propidium iodide (PI) staining buffer (20 μg mL−1 PI (Sigma-Aldrich), 0.2 mg mL−1 RNase A (Thermo Scientific), PBS) for 30 min at room temperature. Cell cycle distribution was analyzed by flow cytometry (BD FACSCanto HTS, BD Biosciences, NJ, USA) and FlowJo software (FlowJo, LLC, OR, USA).

RNA isolation and quantitative RT-PCR

Total RNA was isolated using the Purelink RNA mini kit (Invitrogen, Thermo Fisher Scientific) and treated with Turbo DNA-free kit (Invitrogen, Thermo Fisher Scientific) to purify RNA samples. 1 μg RNA was reverse transcribed using SuperScript III First-Strand Synthesis SuperMix for qRT-PCR (Invitrogen, Thermo Fisher Scientific). Thermal cycler setting: 25°C 10 min, 50°C 30 min, 85°C 5 min, and 37°C 20 min incubation with *E. Coli* RNAse H. Conversely, for miRNA qRT- PCR, reverse transcription was performed using the miRCURY LNA miRNA PCR kit (Qiagen, Hilden, Germany), following the manufacturers' suggestions. A 384-well plate was prepared using Platinum SYBR Green qPCR SuperMix-UDG (Invitrogen, Thermo Fisher Scientific) as a 1:5 dilution of SYBR Green to cDNA. The RT-qPCR was performed by a ViiA 7 Real-Time PCR System with 384-Well Block (Applied Biosystems, Thermo Fisher Scientific; final primer concentration, 100 nM; final volume, 10 μL; thermal profile, 95°C 15 s, 60°C 60 s, 40× cycles). For RNA qRT-PCR, delta Ct (ΔCt) values were calculated by subtracting the Ct values from the genes of interest with the Ct values of the housekeeping genes (*RPL13A*). For miRNA qRT-PCR, the endogenous control utilized was UniSp6. Primer sequences are listed in Table S1.

Co-cultures

Human mesoangioblasts (MABs) were obtained according to the ethics committee approval of the University Hospital Leuven (n° S5732-ML11268). For co-culture experiments, cells were seeded at a 1:20 KMR46:MABs ratio on collagen-coated (Sigma-Aldrich) vessels in IMDM supplemented with 15% FBS, 1% L-glutamine, 1% non-essential amino acids, 1% sodium pyruvate, 1% insulin-transferrin-selenium, 1:10.000 basic fibroblast growth factor and 0.2% beta-mercaptoethanol. All reagents were purchased from Thermo Fisher Scientific. After 24 h (h), medium was changed and Opti-MEM (Gibco, Thermo Fisher Scientific) with miRNA-lipofectamine or lipofectamine (Invitrogen, Thermo Fisher Scientific) was added to the wells. After 24 h, cells were differentiated in DMEM supplemented with 2% horse serum (Gibco, Thermo Fisher Scientific) medium for 96–120 h in 5% O2/5% CO2 at 37°C.

Immunofluorescence

Following our adjusted protocol,[44] cells were first fixed with 4% PFA (Sigma-Aldrich) at room temperature for 10 min. Subsequently, cells were permeabilized with 1% bovine serum albumin (BSA) (Sigma-Aldrich), 0.2% Triton X-100 (Sigma-Aldrich) in PBS (Gibco,

Thermo Fisher Scientific) for 30 min and then blocked in 10% donkey serum (Biowest, Nuaillé, France) for 30 min. Subsequently, cells were incubated with phalloidin solution (Sigma-Aldrich, P1951) diluted 1:500 in PBS with 1% BSA, and nuclei were counterstained with Hoechst 33258(Sigma-Aldrich) at 1 μg/mL. Imaging was performed with a Nikon Eclipse Ti2-A microscope (Nikon, Tokyo, Japan) by means of Image-Pro Plus 6.0 software (Nikon).

RNA-sequencing (RNA-seq)

RNA (>10 μg) samples were verified and processed by the Genomics Core (KU Leuven – UZ Leuven). RNA-seq libraries were constructed with the Lexogen library (Lexogen, Vienna, Austria). Samples were indexed with unique adapters and pooled for single read (50 bp) sequencing in an Illumina HiSeq 2000 sequencer (Illumina, CA, USA). RNA-seq reads were aligned with TopHat v2.0.2 (Johns Hopkins University) to the mouse genome mm10. Transcripts were assessed and quantities were determined by Cufflinks Assembly & DE (Cufflinks38) (Illumina). Differential expression levels were assessed using DESeq2 (Bioconductor).[41] Gene Ontology Biological Process (GO:BP) or KEGG pathways were identified using g:Profiler.[42]

Multiome snRNA-seq/ATAC-seq using chromium 10x genomics platform

Cells were processed according to the 10x Genomics Chromium Single Cell Multiome ATAC+ Gene Expression low cell number protocol conforming to protocol number CG000365_DemonstratedProtocol_NucleiIsolation_ATAC_GEX_Sequencing_RevB used for cell lysis (0.1x lysis buffer and lysed for 6.5 min) to obtain intact nuclei (10x Genomics, CA, USA). Single cell ATAC- and RNA-seq libraries were prepared using the Chromium Single Cell Multiome ATAC + Gene Expression Platform (utilizing the 10x Genomics Single Cell Multiome Kit). Nuclei were prepared and counted to ensure quality and concentration. Nuclei were then transposed according to the manufacturers' protocol. Transposed nuclei suspension was loaded onto the Next GEM Chip J (Chromium Next GEM Chip J Single Cell Kit) targeting 5000 nuclei and then ran on a Chromium Controller instrument to generate GEM emulsion (10x Genomics). Single nuclei gene expression libraries, as well as single nucleiATAC-seq libraries, were generated according to the manufacturers' protocol using the Chromium Next GEM Single Cell Multiome ATAC+ Gene Expression kit (10x Genomics). Final libraries were quantified using the NEBNext Library Quant Kit for Illumina (New England Biolabs, MA, USA) and High Sensitivity D1000 TapeStation (Agilent Technologies, CA, USA). Each library was sequenced separately on a NovaSeq 6000 instrument using an SP 100 cycles reagent kit (Illumina), targeting 25.000 reads/nuclei for ATAC-seq and a minimum of 20.000 reads/nuclei for gene expression. The R packages 'Seurat' (v5.1.0) and 'Signac' (v1.14.0) were used for processing the multiome snRNA-seq/ATAC-seq data.

Tumorsphere assay

20,000 pretreated cells were seeded into Costar 6-well Clear Flat Bottom Ultra-Low Attachment plates (Corning) in serum-free DMEM/F12 (Invitrogen, Thermo Fisher Scientific), supplemented with B-27 Supplement (Gibco, USA), 20 ng/mL EGF (Gibco, Thermo Fisher Scientific), 20 ng/mL bFGF (Gibco, Thermo Fisher Scientific), and 1% Penicillin/Streptomycin (Gibco, Thermo Fisher Scientific). Tumorspheres were imaged and counted at 10 days using an inverted phase-contrast microscope. Tumorspheres with different size ranges were counted as small (25-50um), medium (50-100um), or large (>100um).

miR-eCLIP

24 h after transfection, RD18 cells were crosslinked using a 254 nm UV-C Mercury bulb (UVP Crosslinker CL-3000, Analytik Jena, Jena, Germany). Cells were sent to Eclipse Bioinnovations (CA, USA), where miR-eCLIP was performed.

ATAC-sequencing (ATAC-seq)

ATAC-seq libraries were made as described previously.[45] Briefly, cells were collected and washed with ice-cold PBS (Gibco, Thermo Fisher Scientific), 50.000 cells were pelleted in a pre-cooled 1.5 mL tube by centrifugation for 5 min at 600 rcf at 4°C in a microcentrifuge. The supernatant was removed and 50 μL of ATAC-lysis buffer was added (10 mM Tris-HCl pH 7.4, 10 mM NaCl, 3 mM MgCl2, 0.1% NP40 (all reagents from Sigma-Aldrich)) and the nuclei were pelleted for 10 min at 600 rcf at 4°C in a microcentrifuge. Subsequently, the supernatant was removed and nuclei were resuspended in 50 μL transposition reaction buffer (27.5 μL H2O, 25 μL TD buffer (Sigma-Aldrich), 2.5 μL Tagment DNA Enzyme 1) (Tagment DNA TDE1 Enzyme and Buffer Kit, Illumina, 20034197) and incubated for 30 min at 37°C at 1000 rpm in a thermomixer. The transposed DNA was cleaned up immediately following transposition using the Zymo Research DNA Clean & Concentrator-5 (Capped) kit(Zymo Research, WA, USA, D4014) and amplified in one pre-amplification step (5 cycles) and a final amplification (5–7 cycles) in the same 50 μL reaction using 1x NEBNext High-fidelity 2x PCR Master Mix (New England Biolabs, M0541S). Following amplification, the libraries were purified using the Zymo Research DNA Clean & Concentrator-5 (Capped) kit followed by 0.55x-1.75x dual size selection using the AMPure XP Bead-Based Reagent (Beckman Coulter, CA, USA). The quality of the libraries was assessed using an Agilent Bioanalyzer 2100 with the Agilent High Sensitivity DNA Kit (Agilent Technologies, 5067-4626) and the concentration was determined using the Qubit dsDNA Quantification Assay Kit (Invitrogen, Thermo Fisher Scientific, Q32854). The libraries were diluted to 4 nM and pooled together for SE50 sequencing on an Illumina HiSeq 4000 system, aiming for minimally 25 million mapped and unique reads. ATAC-seq reads were analyzed using the ENCODE ATAC-seq pipeline (https://doi.org/10.5281/zenodo.156534) developed by Anshul Kundaje's laboratory, which performs quality and adapter trimming, alignment, deduplication, peak calling and quality control in a fully automated manner. The resulting peak files and alignment files were used by DiffBind (v3.0.15) (Bioconductor) to find differentially accessible regions (DARs). Profile

plots and heatmaps were made using DeepTools (v3.4.3) (Max Planck Institute for Immunobiology and Epigenetics, Freiburg) from bigwig files generated from merged replicate reads with the ATAC-seq pipeline.

Drug screening

Cells were seeded in 96-well plates (Corning), and 24 h later, tazemetostat (MedChemExpress, NJ, USA, EPZ-6438, HY-13803), doxorubicin (Sigma-Aldrich, D1515-10MG) or topotecan (MedChemExpress, HY-13768) were added at final concentrations of 7μM, 500nM and 500nM, respectively and cell viability was measured at 24h, 48h, 72 h and 96h using the XTT (2,3-Bis-(2-Methoxy-4-Nitro-5-Sulfophenyl)-2H-Tetrazolium-5-Carboxanilide) assay (Invitrogen, Thermo Fisher Scientific, X6493) following the manufacturers' instructions. The vehicle (DMSO) was used as a negative control. Dose-response curves and half maximal inhibitory concentration (IC50) values were calculated using GraphPad Prism (GraphPad Software, CA, USA).

Metabolite extraction and measurements

Metabolite extraction and measurements followed a previously published protocol.[46] Briefly, metabolites for mass spectrometry analysis were previously prepared by quenching the cells in liquid nitrogen followed by a cold two-phase methanol-water-chloroform extraction (Solvent Mixture 20:9:1, Avanti Research, AL, USA). Phase separation was achieved by centrifugation at 4°C. The methanol-water phase containing polar metabolites was separated and dried using a vacuum concentrator. Dried metabolite samples were stored at −80°C. Amino acids and organic acids of the central carbon metabolism were measured with gas chromatography-mass spectrometry. Polar metabolites were derivatized for 90 min at 37°C with 20 μL of 20 mg per mL methoxyamine (Sigma-Aldrich, 226904) in pyridine (Sigma-Aldrich, 270970). Subsequently, 15 μL of N-(tert-butyldimethylsilyl)-N-methyl-trifluoroacetamide with 1% tert-butyldimethylchlorosilane were added to 7.5 μL of each derivative and incubated for 60 min at 60°C (Sigma-Adlrich, 375934).[47] Metabolite concentrations were measured with a 7890A GC system (Agilent Technologies) combined with a 5975C Inert MS system (Agilent Technologies). One μL of sample was injected into a DB35MS column (Agilent Technologies) in split mode (ratio 1 to 3) using an inlet temperature of 270°C. The carrier gas was helium with a flow rate of 1 mL/min. Upon injection, the GC oven was set at 100°C for 1 min and then increased to 105 °C at 2.5 °C/min and with a gradient of 2.5°C/min, finally to 320 °C at 22 °C/min. The measurement of metabolites has been performed under electron impact ionization at 70 eV using a scan mode (mass range 150–650 amu).

Proteomics

Cells were lysed using RIPA lysis buffer (Sigma-Aldrich). Protein concentration was measured using the Pierce BCA Protein Assay Kit (Thermo Fisher Scientific, 23227). Fifty micrograms of protein from each sample were processed for LC/MS analysis using the S-Trap Micro Sample Prep Kit (ProtiFi, https://protifi.com/), adhering to the manufacturer's instructions. Briefly, samples were solubilized in 5% sodium dodecyl sulfate (SDS) in 50 mM triethylammonium bicarbonate (TEAB), reduced with 5 mM tris(2-carboxyethyl)phosphine (TCEP), alkylated with 20 mM iodoacetamide (IAA), and further denatured with 2.5% (v/v) phosphoric acid (all reagents from Sigma-Aldrich). The samples were then applied to S-Trap columns for purification, and proteins were digested with 1 μg trypsin (Trypsin Gold, Mass Spectrometry Grade, Promega, WI, USA) per 50 μg protein. Peptides were sequentially eluted using three different buffers: 1) 50 mM TEAB, 2) 0.2% (v/v) formic acid, and 3) 50% acetonitrile (ACN) (buffers from Sigma-Aldrich). The eluted peptides were then completely dried using a speed vacuum centrifuge. The tryptic peptides were reconstituted in 0.5% ACN, 0.1% formic acid. Approximately 200 ng of the digests were loaded onto an Evotip (Evotip Pure, Evosep, Odense, Denmark). The peptide mixtures were analyzed using an Evosep One LC (Evosep) connected to a ZenoTOF 7600 mass spectrometer equipped with an Optiflow Turbo V ion source (SCIEX, MA, USA). The Evosep One method employed was 60SPD (samples per day), utilizing a 21-min gradient with the EV1109 Performance Column– 60/100 SPD (8 cm × 150 μm, 1.5 μm) (Evosep). The mass spectrometer operated in positive mode with a spray voltage of 4500 V and used SWATH mode. The SWATH acquisition scheme consisted of 65 variable-size windows. All raw data from the ZenoTOF 7600 system (.wiff files) were acquired using the SCIEX OS Software (v3.4.3) and processed with DIA-NN (v1.8.1) (Data-Independent Acquisition by Neural Networks)[48] in library-free mode. Spectra were compared against the Human reference proteome database (https://www.uniprot.org/proteomes/UP000005640) using the following parameters: full tryptic digestion with up to two missed cleavages, oxidation of methionine and N terminus acetylation as variable modifications, and carbamidomethylated cysteines as a fixed modification. Default settings were primarily used, with the exception of a 350–1250 m/z precursor mass range filter, the match between runs (MBR) option was enabled and a mass accuracy setting of 20 ppm for both MS1 and MS2. The neural network classifier was configured for single-pass mode, and protein inference was based on gene information. The quantification strategy employed was robust LC (high precision), cross-run normalization was RT-dependent, and library generation was set to smart profiling. The DIA-NN protein groups output was further analyzed using in-house R scripts (RStudio, Posit, MA, USA). Statistical analyses were performed using RStudio. In order to take into account the values with NA in the proteomic data, we used KNN imputation. LIMMA t test was performed to evaluate the difference in abundance of the proteins between the vehicle and UK-5099 groups. The mass spectrometry proteomics data have been deposited to the ProteomeXchange Consortium via the PRIDE[49] partner repository with the dataset identifier PXD058278.

Oxygen consumption rate

Seahorse XF24 Extracellular Flux Analyzer (Agilent Technologies) was employed to measure oxygen consumption rates (OCR) of FN-RMS and MABs using the Seahorse XF Cell Mito Stress Test Kit (Agilent Technologies) following the manufacturers' protocol. Briefly,

pretreated 30.000 cells/well were plated on Seahorse XF24 V7 PS Cell Culture Microplates (Agilent Technologies) for 14 h in growth medium. Following attachment to the well, medium was changed to XF media (Agilent Technologies) (Seahorse XF DMEM assay medium pack, pH 7.4). Basal OCR was measured for 5 cycles, then 1 μM oligomycin (Sigma-Aldrich, O4876) was injected to inhibit ATP-linked respiration, followed by 2 μM Carbonyl cyanide 4-(trifluoromethoxy)phenylhydrazone (FCCP)(Sigma-Aldrich) to measure maximal respiration and finally, 1 μM Rotenone/Antimycin A from *Streptomyces* sp. (Sigma-Aldrich) was injected to completely inhibit all mitochondrial respiration. After each experiment, protein concentration was measured using the Bradford assay (Quick Start Bradford 1x Dye Reagent, Bio-Rad Laboratories, CA, USA) and wells were normalized using the Wave Desktop software (v2.6) (Agilent Technologies).

Senescence assay

RD18 and KMR46 cells were seeded and treated with DMSO, MPCi, or the miRNA combination (all reagents from Sigma-Aldrich) as described previously (see miRNA/MPCi/siRNA Treatment). For the detection of senescent cells, the β-galactosidase senescence kit from Cell Signaling Technology (MA, USA) was utilized, following manufacturers' instructions. Briefly, cells were fixed using the 1x Fixative Solution supplied in the kit for 10–15 min. Plates were rinsed with 1x PBS (Gibco, Thermo Fisher Scientific) twice and then stained with the β-Galactosidase Staining Solution. Plates were covered with parafilm (Parafilm ''m" laboratory film roll, Bemis Flexible Packaging, WI, USA) and incubated at 37°C overnight, in a dry incubator. Cells were checked for the development of blue color and pictures were taken with a Leica DMi1 inverted microscope (Leica, Wetzlar, Germany). For long term storage, the cells were overlaid with 70% glycerol (Sigma-Aldrich) and stored at 4°C.

Western blot

Western blot analysis was performed on cell lysates in RIPA lysis buffer (Sigma-Aldrich) supplemented with DL-Dithiothreitol (DTT, 1:100) (Sigma-Aldrich), Phosphatase Inhibitor Cocktail 3 (1:100) (Sigma-Aldrich), and Sodium orthovanadate (1:100) (Sigma-Aldrich). Equal amounts of protein (20 μg) (Quick Start Bradford 1x Dye Reagent, Bio-Rad Laboratories) were denatured in sample loading buffer (50 mM Tris–HCl, pH 6.8, 100 mM DTT, 2% SDS, 0.1% bromophenol blue, 10% glycerol for 10 min at 95°C (all reagents from Sigma-Aldrich)). Samples were run on hand-casted SDS polyacrylamide gels and transferred to nitrocellulose membranes (Amersham Protran 0.45 NC nitrocellulose Western blotting membranes, Cytiva, MA, USA)). The membranes were blocked in 5% skim milk (Sigma-Aldrich) made in Tris-buffered saline (TBS) (Sigma-Aldrich) containing 0.05% Tween (Sigma-Aldrich) for 1 h and incubated overnight with primary antibody (MYF5 (Myf-5 (C-20), Santa Cruz Biotechnology, CA, USA, sc-302) 1:500, MYOG (in-house hybridoma) 1:3, anti-FAK (Sigma Aldrich, 06–543) 1:500, anti-P-FAK (Anti-phospho-Focal Adhesion Kinase (Tyr397), clone 18, Sigma Aldrich,05–1140) 1:500, VE-CADHERIN (Mouse VE-Cadherin,R&D Systems, MN, USA,Af-1002) 1:1000, GAPDH (Anti-GAPDH antibody produced in rabbit, Sigma-Aldrich, G9545) 1:1000, Alpha Tubulin (Monoclonal Anti-α-Tubulin antibody produced in mouse, Sigma-Aldrich, T5168) 1:1000. Following secondary antibody incubations with 1:5000 anti-mouse (Goat Anti-Mouse IgG (H + L)- horseradish peroxidase (HRP) Conjugate,Bio-Rad Laboratories, 1706516), anti-rabbit (Goat Anti-Rabbit IgG (H + L)-HRP Conjugate,Bio-Rad Laboratories, 1706515) and anti-goat (Rabbit Anti-Goat IgG (H + L)-HRP Conjugate, # (Bio-Rad Laboratories, 1721034) in 2.5% skim milk for 1 h. Membranes were developed using SuperSignal Femto or Pico substrates (SuperSignal West Femto Maximum Sensitivity Substrate, SuperSignal West Pico PLUS Chemiluminescent Substrate, Thermo Scientific) and bands were detected with a ChemiDoc XRS+ Gel Doc XR + System detection system (Bio-Rad Laboratories).

Reporter cell line

Cells were transduced with lentiviral particles expressing elongation factor 1-alpha-enhanced green fluorescent protein-porcine teschovirus-1-firefly luciferase (EF1a-eGFP-P2A-fLuc) (Addgene, MA, USA) and selected with 1 μg/mL Puromycin Dihydrochloride (Gibco, Thermo Fisher Scientific) for 2 weeks. GFP was used as a standard gene expression tracer *in vitro*. fLuc was used as an optical reporter gene, upon coelenterazine administration, to detect the cell line engraftment *in vivo* via IVIS bioluminescence imaging (BLI) (IVIS Spectrum, PerkinElmer, MA, USA).

Bioluminescence imaging and treadmill exhaustion test

Mice were monitored through BLI assay at day 5, 10, 12, 14, 16, 18, 20 and 22 after tumor injection using IVIS Spectrum (PerkinElmer). D-luciferin (Promega) was injected subcutaneously at a concentration of 126 mg/kg[50] and consecutive frames were acquired until the maximum signal intensity was reached. Pulse/sec intensities were calculated by comparing the same region of interest (ROI) for all the animals, after subtracting the background signal coming from non-injected mice.

The treadmill exhaustion test was performed at days 5, 10, 15, 20 and 25 after the beginning of the experiment (day 0). The electric shock frequency and intensity were pulses of 200 ms/pulse of electric current with 2 pulse/s repetition rate (3 Hz) and intensity (1.22 mA), as per the protocol from our group.[51] The mice were introduced to the treadmill belt and an adaptation time of 5 min was given before the recordings (motor speed set to zero, for 5 min). A training time of 2 min at 4 m/min was set. Later, the motor speed was set to 7 m/min, with a 1 m/min increase and a constant uphill inclination of 20°, until exhaustion and >10 s stop. The mice were weighted immediately after every run. Speed (m/min), distance (m), and time (min and s) were registered and used for calculating the work of each run in Joules (J). The formula applied was: Work (J) = body mass (kg) × gravity (9.81 m = s2) × vertical speed (m/s × angle) × time (s). For the *ex vivo* analysis, prior to euthanasia mice were injected at 150 mg/kg with 15 mg/mL stock of D-luciferin (Promega).

After necropsy, lungs were placed individually into wells of a 24-well plate (Corning) and D-luciferin (300 μg/mL) was added to cover the tissues. Tissues were imaged at 1 min of exposure.

Hematoxylin and eosin

The procedure for haematoxylin and eosin staining followed previously published methods.[52] Briefly, cryosections were immersed in PBS for 10 min, followed by staining with Harris haematoxylin (Sigma-Aldrich) for 2 min and washing in running water for 2 min. The sections were then sequentially treated (each for 1 min) with acid alcohol (Sigma-Aldrich), running water, bluing reagent (Biognost, Zagreb, Croatia), running water, eosin (Sigma-Aldrich), 95% ethanol, 100% ethanol (Sigma-Aldrich), and xylene (Sigma-Aldrich), before being mounted with dibutylphthalate polystyrene xylene (DPX) (DPX Mountant for histology, Sigma-Aldrich) and left on a slide heater overnight. Images were captured using a Zeiss Axio Imager Z1 (Zeiss, Jena, Germany).

QUANTIFICATION AND STATISTICAL ANALYSIS

All statistical analyses were conducted using GraphPad Prism v10.3.0 (GraphPad Software). Depending on the variables of the experiment, two tailed unpaired Student's t-test analysis or two-way ANOVA test was performed. Statistical details of the experiments can be found in the respective figure legends, including the statistical tests used, exact value of n, what n represents. Data are represented as mean ± SD.

Cell Reports, Volume *44*

Supplemental information

miR-449a/miR-340 reprogram cell identity and metabolism in fusion-negative rhabdomyosarcoma

Enrico Pozzo, Laura Yedigaryan, Nefele Giarratana, Chao-chi Wang, Gabriel Miró Garrido, Ewoud Degreef, Vittoria Marini, Gianmarco Rinaldi, Bernard K. van der Veer, Gabriele Sassi, Guy Eelen, Mélanie Planque, Alessandro Fanzani, Kian Peng Koh, Peter Carmeliet, Jason T. Yustein, Sarah-Maria Fendt, Anne Uyttebroeck, and Maurilio Sampaolesi

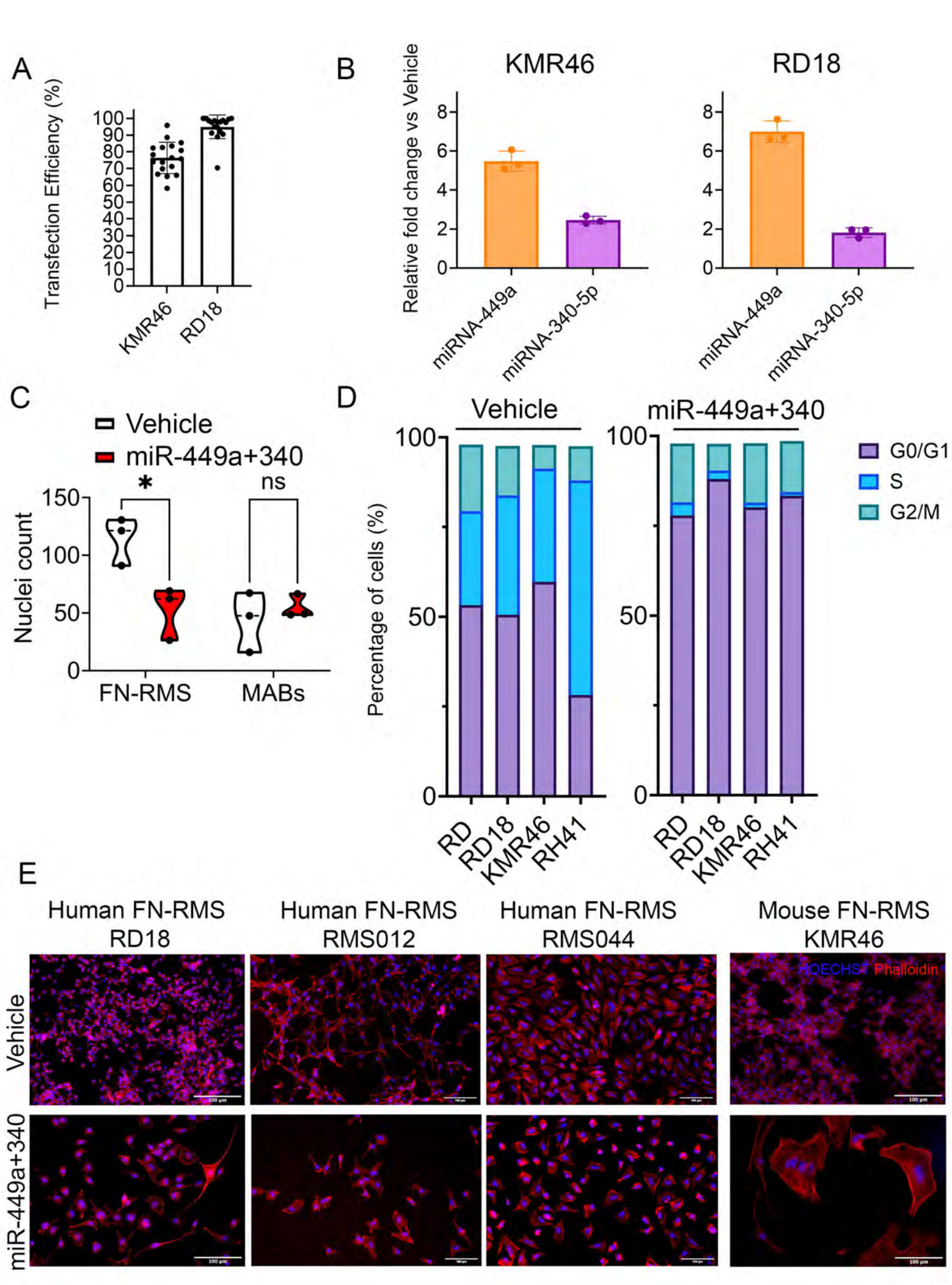
A
Transfection Efficiency (%)
KMR46
RD18
B
KMR46
RD18
Relative fold change vs Vehicle
miRNA-449a
miRNA-340-5p
C
Vehicle
miR-449a+340
Nuclei count
FN-RMS
MABs
*
ns
D
Vehicle
miR-449a+340
Percentage of cells (%)
G0/G1
S
G2/M
RD
RD18
KMR46
RH41
E
Human FN-RMS RD18
Human FN-RMS RMS012
Human FN-RMS RMS044
Mouse FN-RMS KMR46
HOECHST Phalloidin
Vehicle
miR-449a+340

Figure S1. **miR-449a and miR-340 effects, related to Figure 2**. (A) Transfection efficiency at 24 hours of KMR46 and RD18 assessed using FAM3™ Dye-Labeled Pre-miR Negative Control (n=18); (B) Quantitative real-time PCR to assess the overall expression of miRNAs after transfection (n=3); (C) Quantitative effect of miRNAs on murine FN-RMS proliferation in a co-culture setting with human MABs compared to vehicle (n=3). Data presented as mean +/- SD, unpaired t-test. *$p<0.05$, ns not significant; (D) EdU analysis of FN-RMS (RD, RD18, KMR46) and FP-RMS (RH41) cell lines after transfection with miR-499a+340 (n>3); (E) Representative images of immunofluorescence of FN-RMS after miRNA transfection in human and murine FN-RMS cell models. Nuclei are counterstained with Hoechst (blue). Phalloidin (red). Scale bar = 100μm.

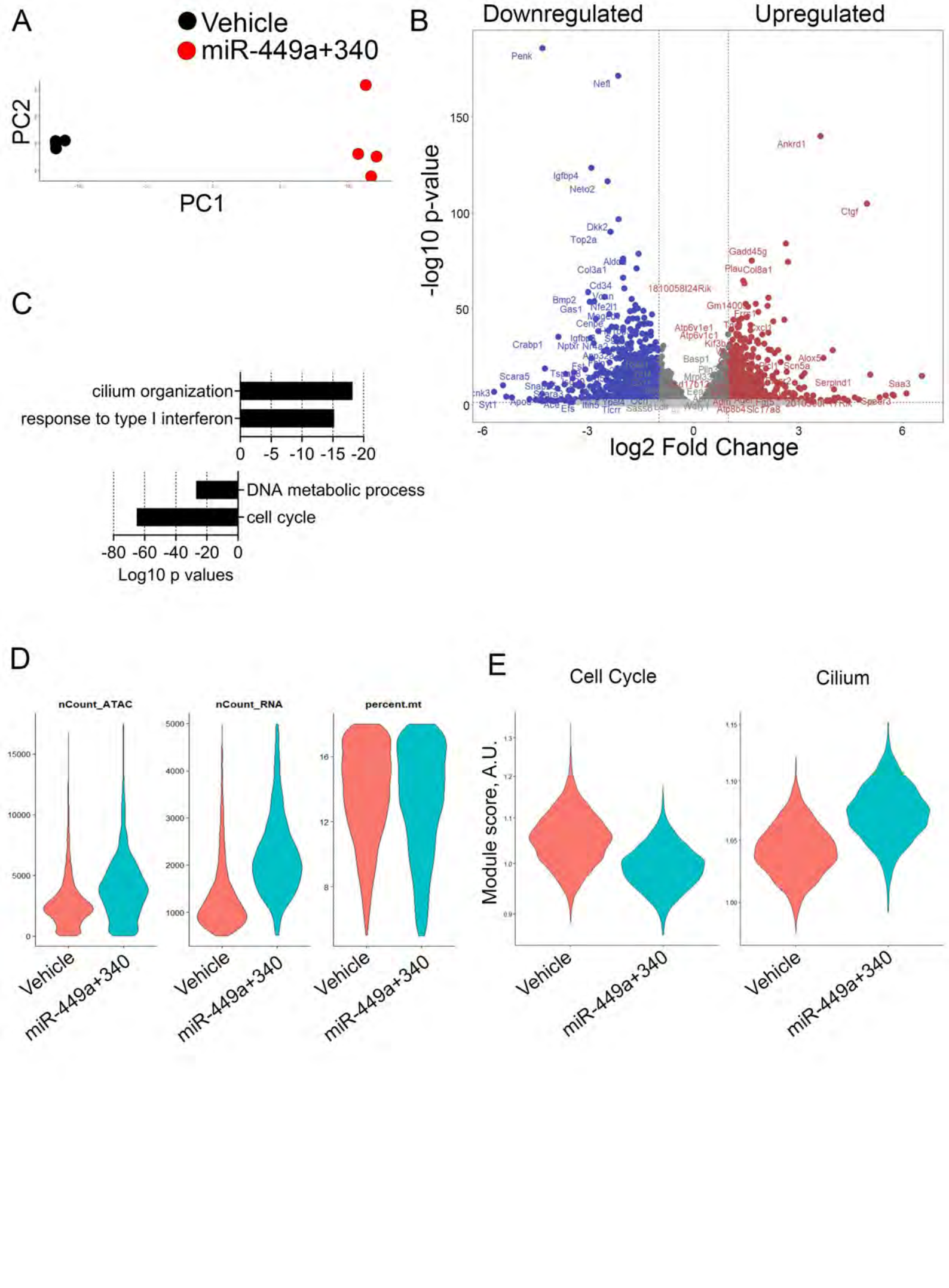
A
Vehicle
miR-449a+340
PC2
PC1
B
Downregulated
Upregulated
-log10 p-value
log2 Fold Change
Penk
Nefl
Ankrd1
Igfbp4
Neto2
Ctgf
Dkk2
Top2a
Gadd45g
Col3a1
Col8a1
Cd34
Bmp2
Gas1
Crabp1
Scara5
Alox5
Scn5a
Serpind1
Saa3
C
cilium organization
response to type I interferon
DNA metabolic process
cell cycle
Log10 p values
D
nCount_ATAC
nCount_RNA
percent.mt
Vehicle
miR-449a+340
E
Cell Cycle
Cilium
Module score, A.U.
Vehicle
miR-449a+340

Figure S2. Transcriptome and epigenome effect of miR-449a and miR-340, related to Figure 2 (A) Principal component and (B) Volcano plot of upregulated (red) and downregulated (blue) genes in vehicle- versus miRNA-transfected murine FN-RMS cell line KMR46 (n=4); (C) Top Gene Ontology Biological Processes (GO:BP) pathways based on the upregulated and downregulated genes from the RNAseq of human FN-RMS cell lines after miRNA transfection (n=4); (D) Violin plots representing the number of unique transcripts per cell for ATAC, RNA and percent.mt in the snRNAseq/ATACseq of human FN-RMS cell line after miRNA transfection (6688 cells); (E) Relative abundance of cell cycle- and cilium-related genes in the snRNAseq of human FN-RMS cell line after miRNA perturbation compared to vehicle.

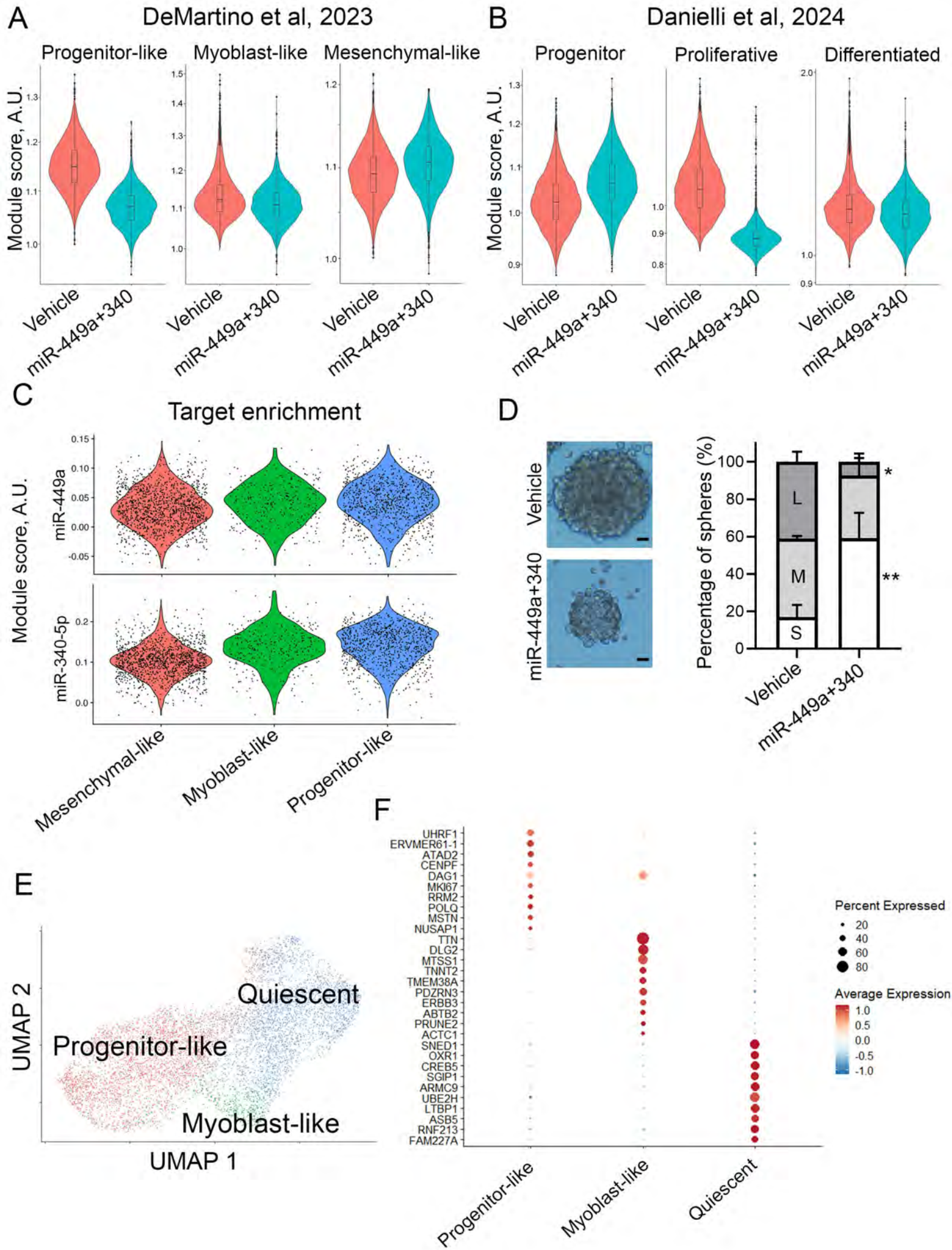
A
DeMartino et al, 2023
Progenitor-like
Myoblast-like
Mesenchymal-like
Module score, A.U.
Vehicle
miR-449a+340
B
Danielli et al, 2024
Progenitor
Proliferative
Differentiated
C
Target enrichment
miR-449a
miR-340-5p
Mesenchymal-like
Myoblast-like
Progenitor-like
D
Vehicle
miR-449a+340
Percentage of spheres (%)
L
M
S
*
**
E
UMAP 2
UMAP 1
Quiescent
Progenitor-like
Myoblast-like
F
UHRF1
ERVMER61-1
ATAD2
CENPF
DAG1
MKI67
RRM2
POLQ
MSTN
NUSAP1
TTN
DLG2
MTSS1
TNNT2
TMEM38A
PDZRN3
ERBB3
ABTB2
PRUNE2
ACTC1
SNED1
OXR1
CREB5
SGIP1
ARMC9
UBE2H
LTBP1
ASB5
RNF213
FAM227A
Percent Expressed
Average Expression
Progenitor-like
Myoblast-like
Quiescent

Figure S3. Cell identity shift of FN-RMS after miR-449a+340, related to Figure 2. Genes used to identify the cell states in the papers of (A) DeMartino et al and (B) Danielli et al were used as vectors to calculate the cell states' relative abundance in the snRNAseq of human FN-RMS cell line after miRNA perturbation compared to vehicle; (C) Expression of the genes targeted by miR-449a (top) and miR-340 (bottom) in the samples used in the study by DeMartino et al; (D) Representative images of RD18 tumorspheres (left) and quantification of size distributions (right), scale bar = 20μm (n=3). Data presented as mean +/- SD, two-way ANOVA. *$p<0.05$, **$p<0.01$; (E) Identification of cell states from the snRNA-seq of human FN-RMS cell line after miRNA perturbation compared to vehicle (6688 cells); (F) Selection of genes characterizing the subpopulations in the snRNAseq analysis of vehicle and miR-449a+340 FN-RMS.

A

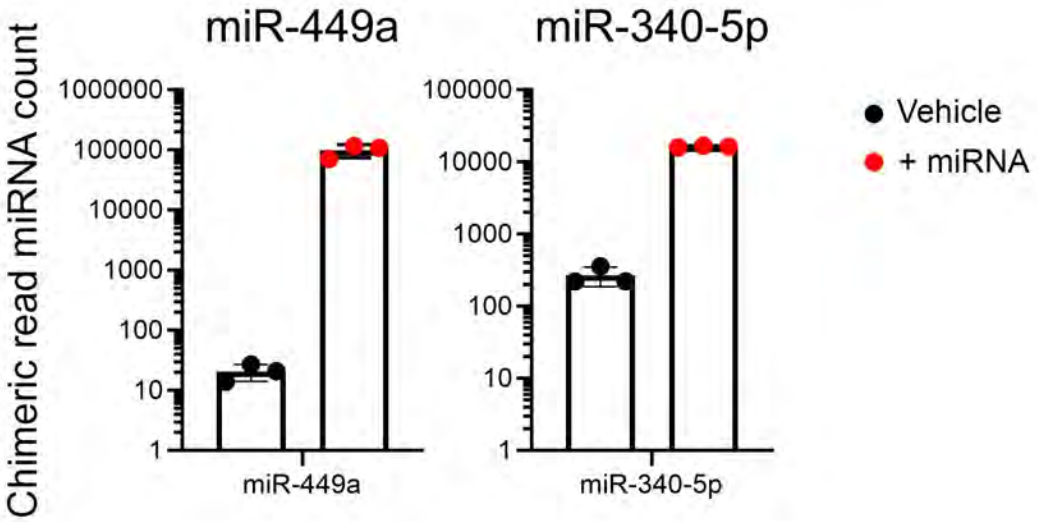
miR-449a
miR-340-5p
Chimeric read miRNA count
1000000
100000
10000
1000
100
10
1
miR-449a
miR-340-5p
Vehicle
+ miRNA

B

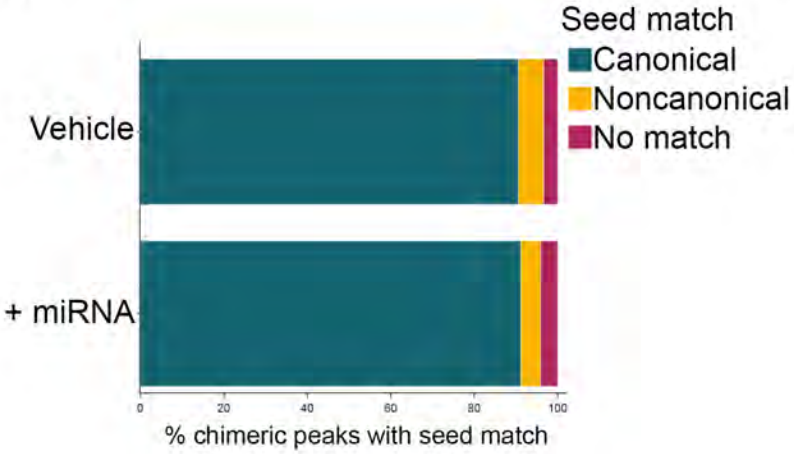
Seed match
Canonical
Noncanonical
No match
Vehicle
+ miRNA
0
20
40
60
80
100
% chimeric peaks with seed match

C

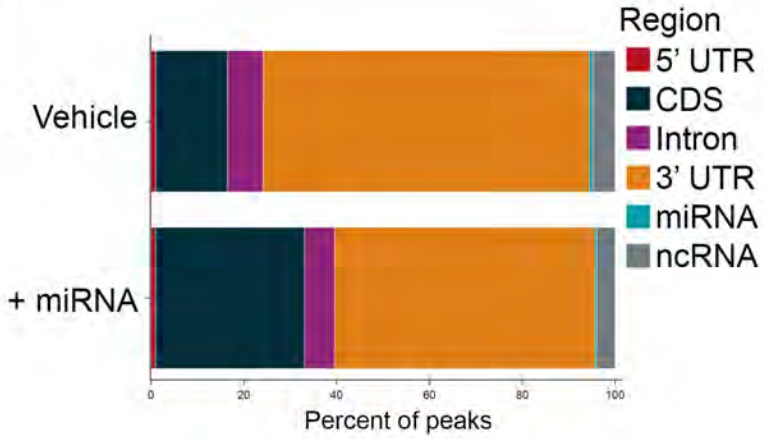
Region
5' UTR
CDS
Intron
3' UTR
miRNA
ncRNA
Vehicle
+ miRNA
0
20
40
60
80
100
Percent of peaks

D

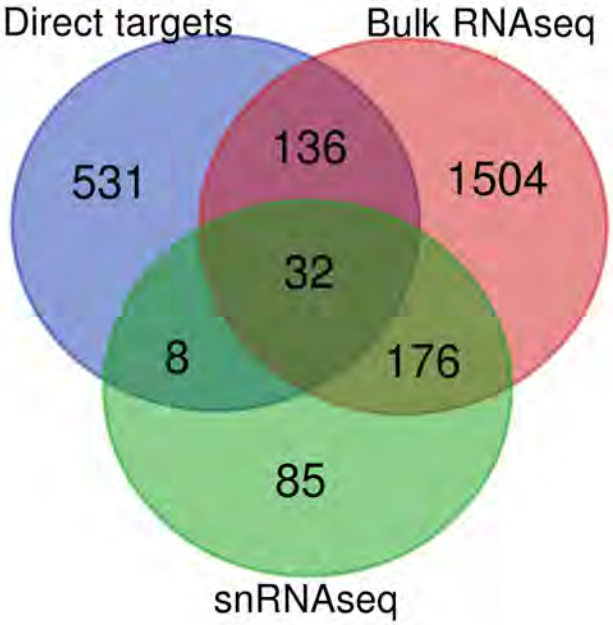
Direct targets
Bulk RNAseq
snRNAseq
531
136
1504
32
8
176
85

Figure S4. eCLIP analysis, related to Figure 3. (A) Chimeric reads for miR-449a and miR-340-5p after eCLIP (n=3 per condition); (B) Seed match distribution of miRNA target peaks and reproducible miRNA target peaks for each set of sample conditions with "Canonical" (i.e., 7mer-m8 or 7mer-1A or 8mer or 6mer positions) and “Noncanonical” (6mer offset or 3' compensatory site or centered site) seed matches; (C) Feature distribution of miRNA target peaks in each sample, as well as reproducible miRNA target peaks for each set of replicates. Sites are annotated according to the following hierarchy: CDS, 5'UTR or 3'UTR, miRNA, intron, ncRNA (non-coding RNA) and other; (D) Venn diagram showing the overlap between direct targets as identified by miR-eCLIP, genes found to be downregulated in bulk RNAseq and genes in the snRNAseq analysis.

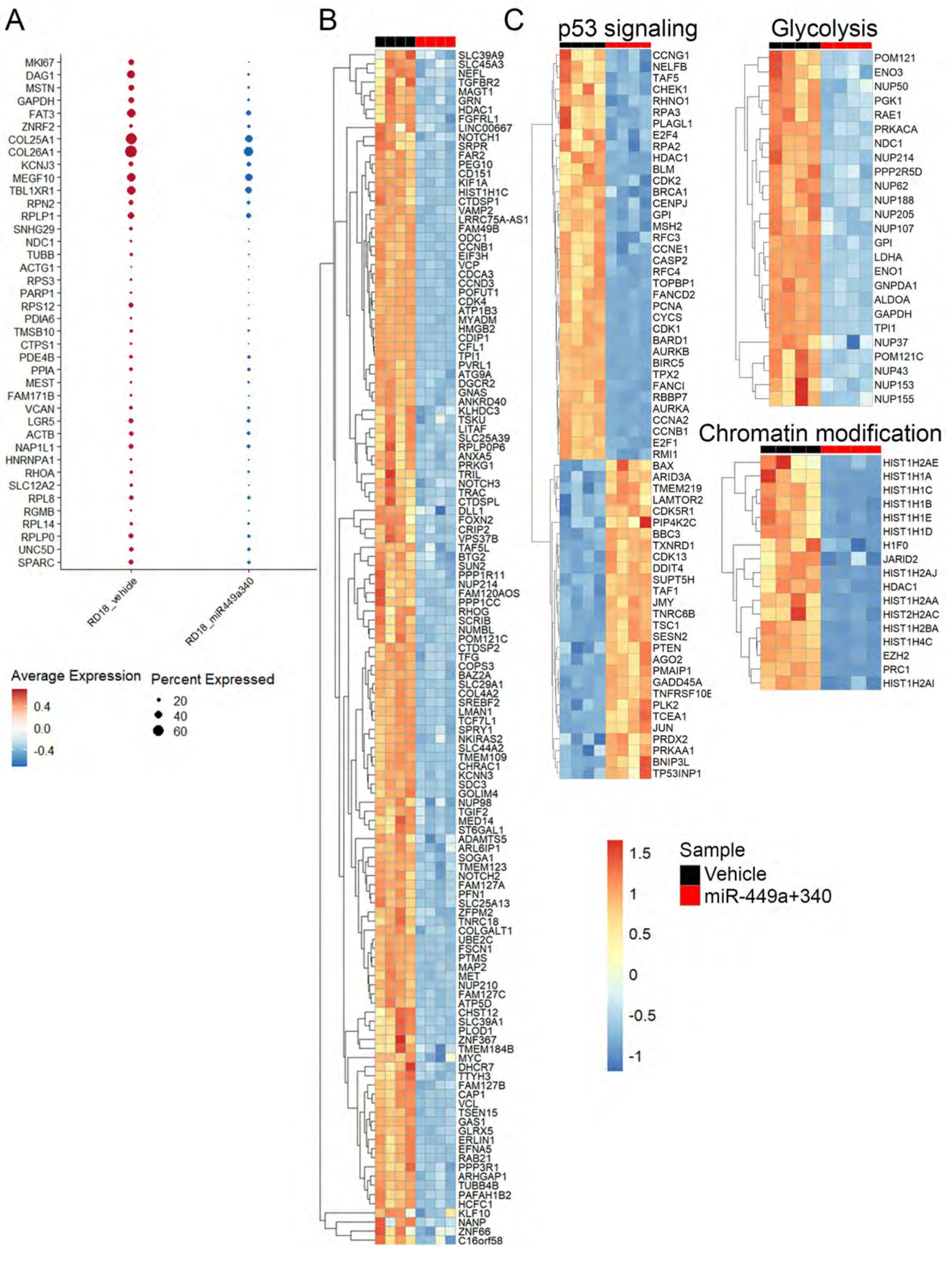
A
MKI67
DAG1
MSTN
GAPDH
FAT3
ZNRF2
COL25A1
COL26A1
KCNJ3
MEGF10
TBL1XR1
RPN2
RPLP1
SNHG29
NDC1
TUBB
ACTG1
RPS3
PARP1
RPS12
PDIA6
TMSB10
CTPS1
PDE4B
PPIA
MEST
FAM171B
VCAN
LGR5
ACTB
NAP1L1
HNRNPA1
RHOA
SLC12A2
RPL8
RGMB
RPL14
RPLP0
UNC5D
SPARC
RD18_vehicle
RD18_miR449a340
Average Expression
0.4
0.0
-0.4
Percent Expressed
20
40
60
B
SLC39A9
SLC45A3
NEFL
TGFBR2
MAGT1
GRN
HDAC1
FGFRL1
LINC00667
NOTCH1
SRPR
FAR2
PEG10
CD151
KIF1A
HIST1H1C
CTDSP1
VAMP2
LRRC75A-AS1
FAM49B
ODC1
CCNB1
EIF3H
VCP
CDCA3
CCND3
POFUT1
CDK4
ATP1B3
MYADM
HMGB2
CDIP1
CFL1
TPI1
PVRL1
ATG9A
DGCR2
GNAS
ANKRD40
KLHDC3
TSKU
LITAF
SLC25A39
RPLP0P6
ANXA5
PRKG1
TRIL
NOTCH3
TRAC
CTDSPL
DLL1
FOXN2
CRIP2
VPS37B
TAF5L
BTG2
SUN2
PPP1R11
NUP214
FAM120AOS
PPP1CC
RHOG
SCRIB
NUMBL
POM121C
CTDSP2
TFG
COPS3
BAZ2A
SLC29A1
COL4A2
SREBF2
LMAN1
TCF7L1
SPRY1
NKIRAS2
SLC44A2
TMEM109
CHRAC1
KCNN3
SDC3
GOLIM4
NUP98
TGIF2
MED14
ST6GAL1
ADAMTS5
ARL6IP1
SOGA1
TMEM123
NOTCH2
FAM127A
PFN1
SLC25A13
ZFPM2
TNRC18
COLGALT1
UBE2C
FSCN1
PTMS
MAP2
MET
NUP210
FAM127C
ATP5D
CHST12
SLC39A1
PLOD1
ZNF367
TMEM184B
MYC
DHCR7
TTYH3
FAM127B
CAP1
VCL
TSEN15
GAS1
GLRX5
ERLIN1
EFNA5
RAB21
PPP3R1
ARHGAP1
TUBB4B
PAFAH1B2
HCFC1
KLF10
NANP
ZNF66
C16orf58
C
p53 signaling
CCNG1
NELFB
TAF5
CHEK1
RHNO1
RPA3
PLAGL1
E2F4
RPA2
HDAC1
BLM
CDK2
BRCA1
CENPJ
GPI
MSH2
RFC3
CCNE1
CASP2
RFC4
TOPBP1
FANCD2
PCNA
CYCS
CDK1
BARD1
AURKB
BIRC5
TPX2
FANCI
RBBP7
AURKA
CCNA2
CCNB1
E2F1
RMI1
BAX
ARID3A
TMEM219
LAMTOR2
CDK5R1
PIP4K2C
BBC3
TXNRD1
CDK13
DDIT4
SUPT5H
TAF1
JMY
TNRC6B
TSC1
SESN2
PTEN
AGO2
PMAIP1
GADD45A
TNFRSF10B
PLK2
TCEA1
JUN
PRDX2
PRKAA1
BNIP3L
TP53INP1
Glycolysis
POM121
ENO3
NUP50
PGK1
RAE1
PRKACA
NDC1
NUP214
PPP2R5D
NUP62
NUP188
NUP205
NUP107
GPI
LDHA
ENO1
GNPDA1
ALDOA
GAPDH
TPI1
NUP37
POM121C
NUP43
NUP153
NUP155
Chromatin modification
HIST1H2AE
HIST1H1A
HIST1H1C
HIST1H1B
HIST1H1E
HIST1H1D
H1F0
JARID2
HIST1H2AJ
HDAC1
HIST1H2AA
HIST2H2AC
HIST1H2BA
HIST1H4C
EZH2
PRC1
HIST1H2AI
1.5
1
0.5
0
-0.5
-1
Sample
Vehicle
miR-449a+340

Figure S5. Direct targets and downstream genes after miR-449a+340, related to Figure 3. (A) List of direct targets found to be downregulated in snRNAseq and (B) bulk RNAseq analysis 60 hours after miR-449a+340 transfection (n=4 per condition); (C) Heatmap of genes in bulk RNAseq analysis after miR-449a+340 transfection related to glycolysis, p53 signaling and chromatin modification according to KEGG pathways (n=4 per condition).

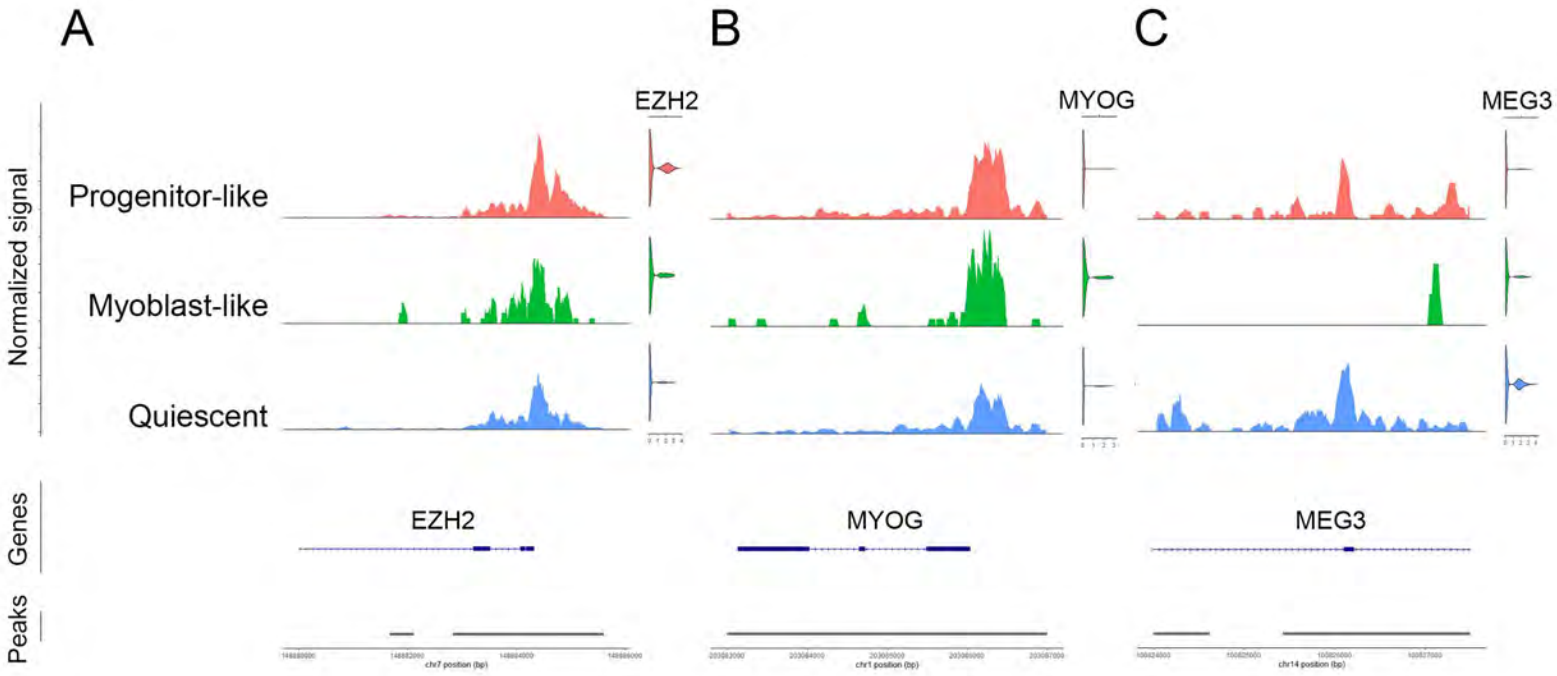
A
B
C
EZH2
MYOG
MEG3
Normalized signal
Progenitor-like
Myoblast-like
Quiescent
Genes
Peaks
EZH2
MYOG
MEG3

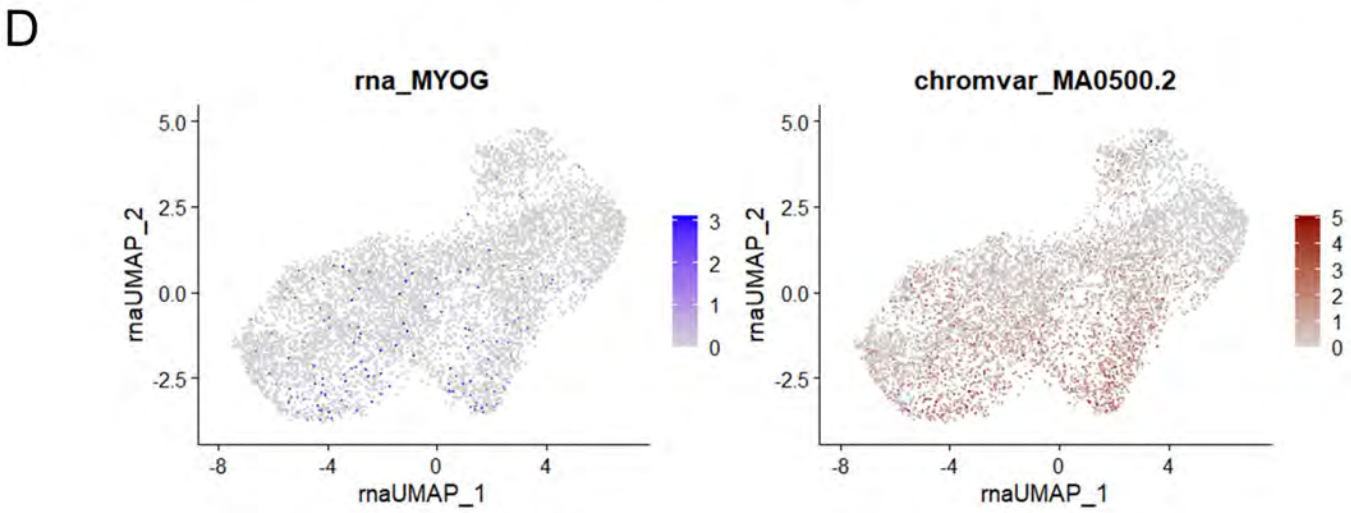
D
rna_MYOG
chromvar_MA0500.2
rnaUMAP_2
rnaUMAP_1
5.0
2.5
0.0
-2.5
-8
-4
0
4
3
2
1
0
5
4
3
2
1
0

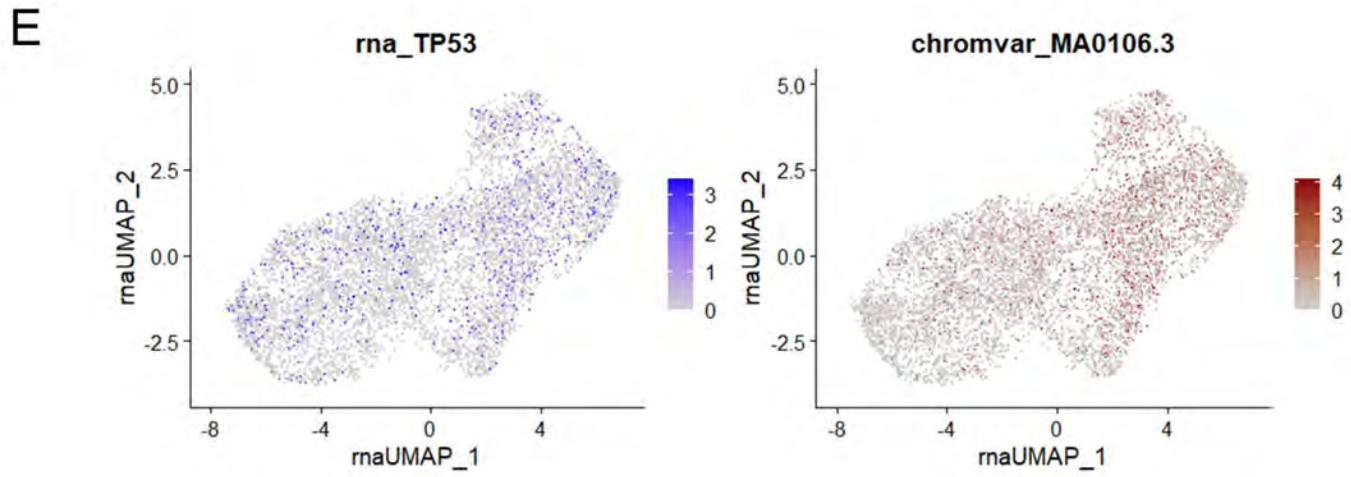
E
rna_TP53
chromvar_MA0106.3
rnaUMAP_2
rnaUMAP_1
5.0
2.5
0.0
-2.5
-8
-4
0
4
3
2
1
0
4
3
2
1
0

Figure S6. Chromatin accessibility at snATACseq, related to Figure 3. snATACseq of human FN-RMS cell line after miRNA perturbation compared to vehicle, showing change in accessibility of (A) EZH2, (B) MYOG and (C) MEG3 after miRNA transfection (6688 cells); (D) expression of *MYOG* and (E) *TP53* using snRNAseq (left), and their motif enrichment in the snATACseq (right).

A

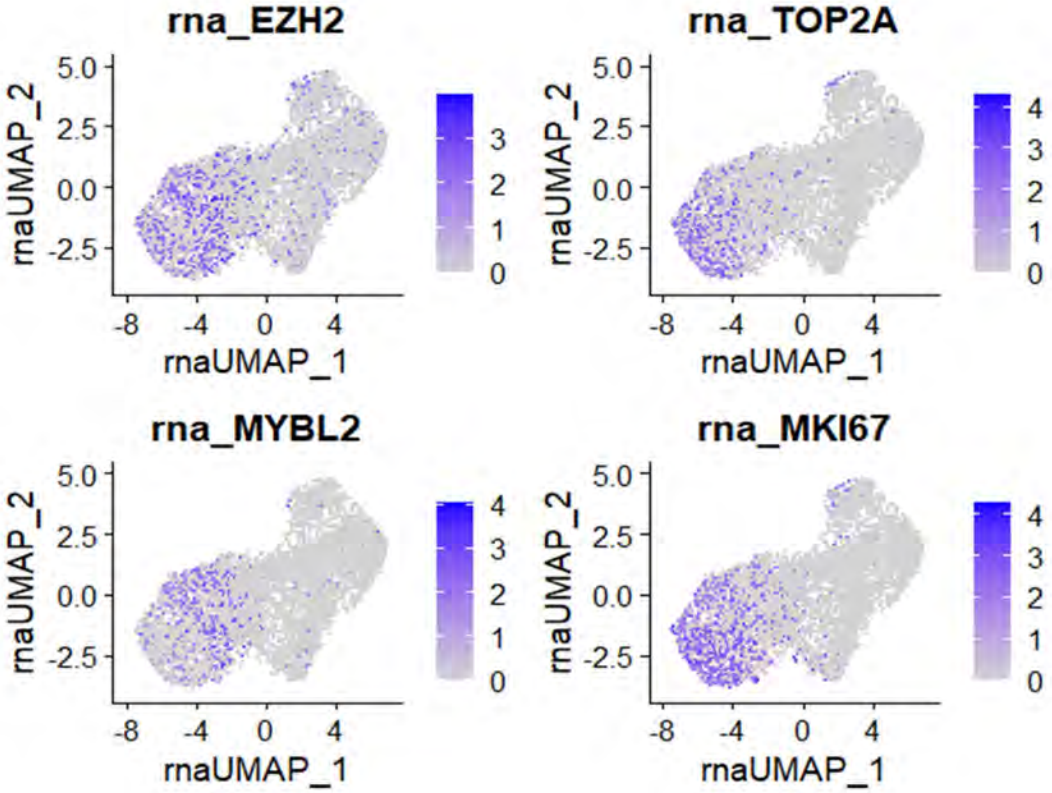
rna_EZH2
rna_TOP2A
rna_MYBL2
rna_MKI67
rnaUMAP_1
rnaUMAP_2

B

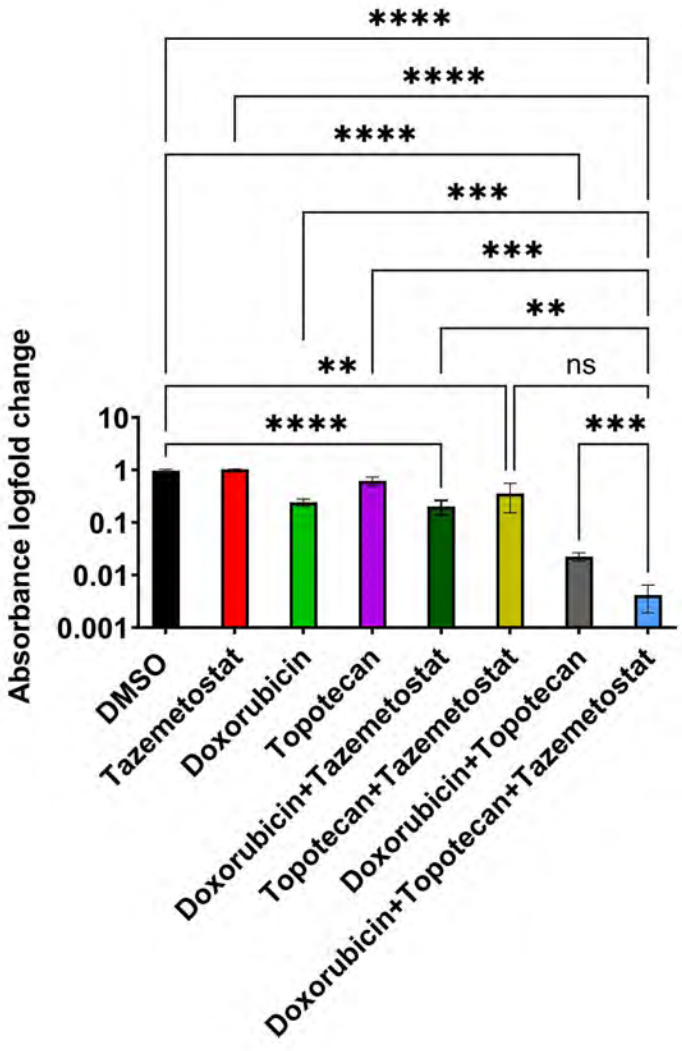
Absorbance logfold change
DMSO
Tazemetostat
Doxorubicin
Topotecan
Doxorubicin+Tazemetostat
Topotecan+Tazemetostat
Doxorubicin+Topotecan
Doxorubicin+Topotecan+Tazemetostat
ns

Figure S7. Synergistic effect of drugs targeting EZH2, TOP2A and MYBL2, related to Figure 3. (A) Expression of EZH2, TOP2A, MYBL2 and MKI67 in the snRNAseq data; (B) XTT proliferation assay of human FN-RMS after 96 hours of treatment with tazemetostat (EZH2 inhibitor), doxorubicin (TOP2A inhibitor) and topotecan (MYBL2 inhibitor) (n>5). Data presented as mean +/- SD, one-way ANOVA. *p<0.05, **p<0.01, ***p<0.001, ****p<0.0001.

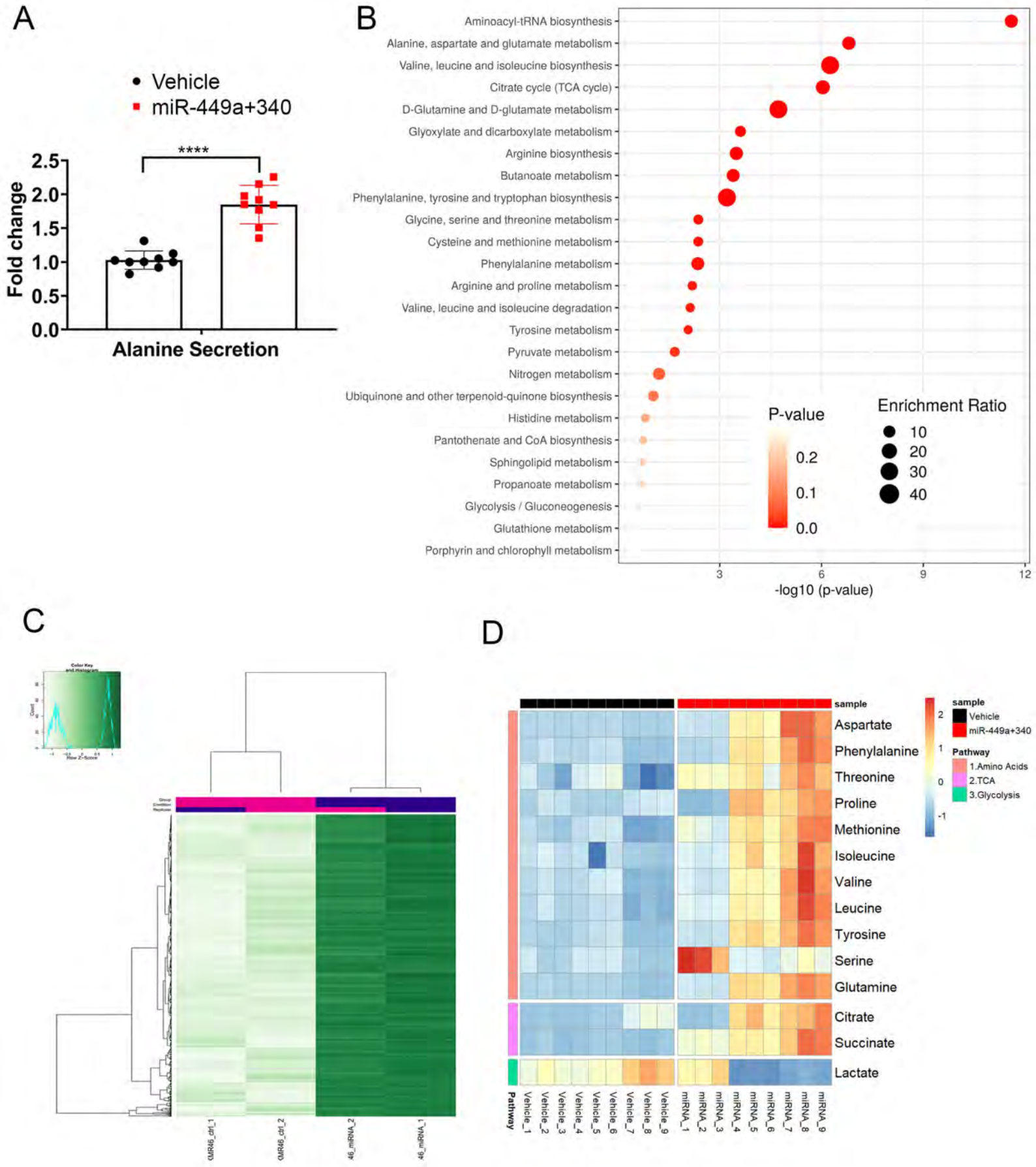

Supplementary figure 9

Figure S8. Metabolomic analysis, related to Figure 3. (A) Extracellular measurement of alanine in human FN-RMS after miRNA transfection compared to vehicle (n=8). Data presented as mean +/- SD, unpaired t-test. ****p<0.0001.; (B) Top 25 enriched KEGG pathways of the intracellular metabolites in human FN-RMS after miRNA transfection, identified using Metaboanalyst; (C) Heatmap of bulk ATAC-seq analysis of murine FN-RMS cell line after miRNA transfection compared to vehicle (n=2); (D) Intracellular metabolite accumulation in murine FN-RMS cell line after miRNA transfection. Statistically significant ($p<0.05$) metabolite and their log-fold change are shown (n=9).

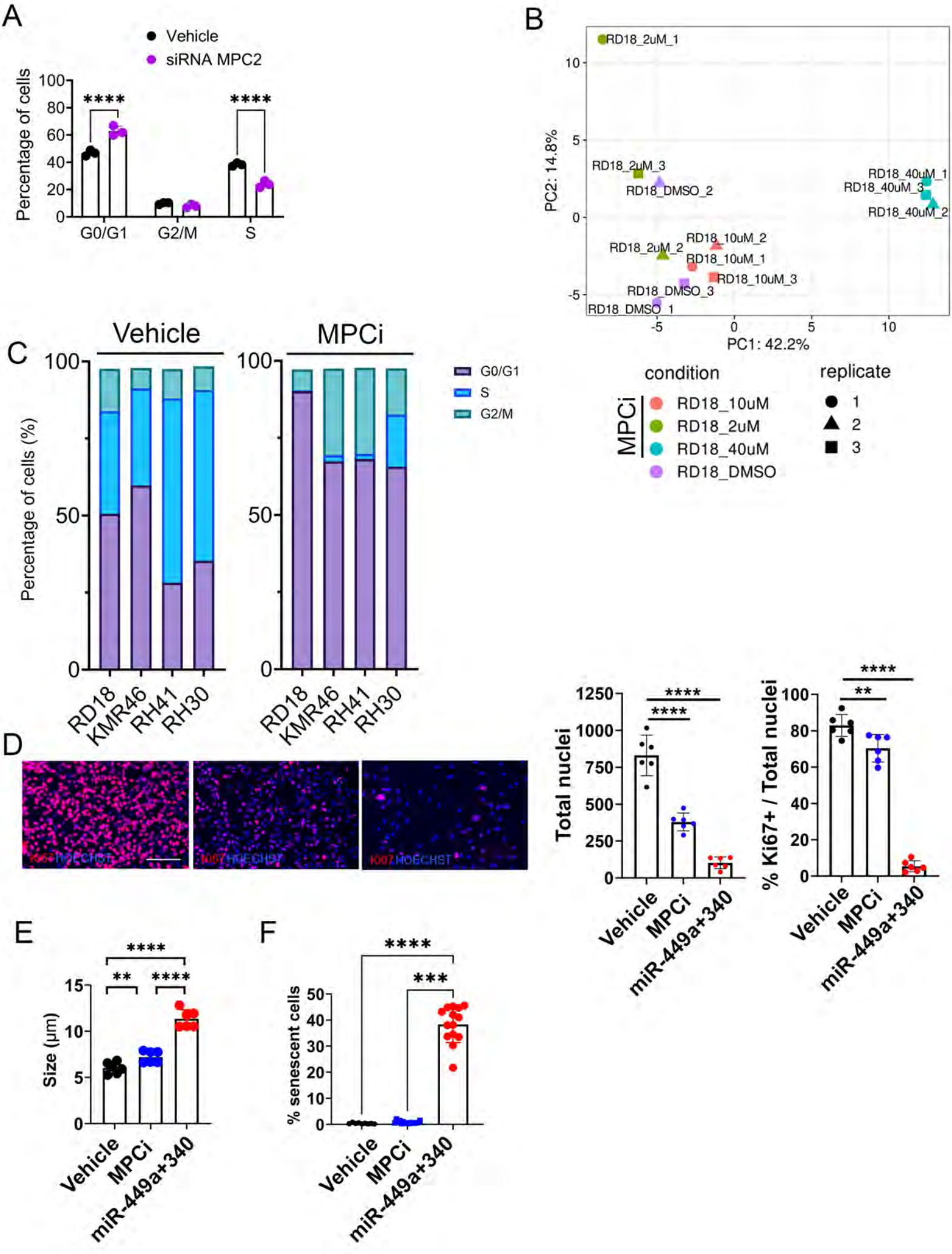
A
Vehicle
siRNA MPC2
Percentage of cells
****
****
G0/G1
G2/M
S
B
RD18_2uM_1
RD18_2uM_3
RD18_DMSO_2
RD18_40uM_1
RD18_40uM_3
RD18_40uM_2
RD18_2uM_2
RD18_10uM_2
RD18_10uM_1
RD18_10uM_3
RD18_DMSO_3
RD18_DMSO_1
PC2: 14.8%
PC1: 42.2%
condition
MPCi
RD18_10uM
RD18_2uM
RD18_40uM
RD18_DMSO
replicate
1
2
3
C
Vehicle
MPCi
Percentage of cells (%)
G0/G1
S
G2/M
RD18
KMR46
RH41
RH30
D
Ki67/HOECHST
Total nuclei
****
****
Vehicle
MPCi
miR-449a+340
% Ki67+ / Total nuclei
****
**
Vehicle
MPCi
miR-449a+340
E
Size (µm)
**
****
****
Vehicle
MPCi
miR-449a+340
F
% senescent cells
****
***
Vehicle
MPCi
miR-449a+340

Figure S9. Effects of MPC inhibition, related to Figure 4. (A) EdU analysis of human FN-RMS cell line after transfection with siRNAs targeting MPC2 (n=3). Data presented as mean +/- SD, unpaired t-test. ****p<0.0001; (B) Principal component analysis of proteomic performed after FN-RMS cell line treatment with UK-5099 at several concentrations (n=3 per conditions); (C) EdU analysis of FN-RMS (RD18, KMR46) and FP-RMS (RH41, RH30) after MPCi (UK-5099) at 40 μM (n=5); (D) Representative immunofluorescence of human FN-RMS after miRNA or MPCi perturbation compared to vehicle (left), with quantification of Ki67 percentage ratio on total number of nuclei (right). Nuclei are counterstained with Hoechst (blue). Ki67 (red). (n=3); (E) Size and (F) percentage of senescent cells in human FN-RMS after miR-449a+340 or MPCi perturbation (n=3). Data presented as mean +/- SD, one-way ANOVA.**p<0.01, ***p<0.001, ****p<0.0001.

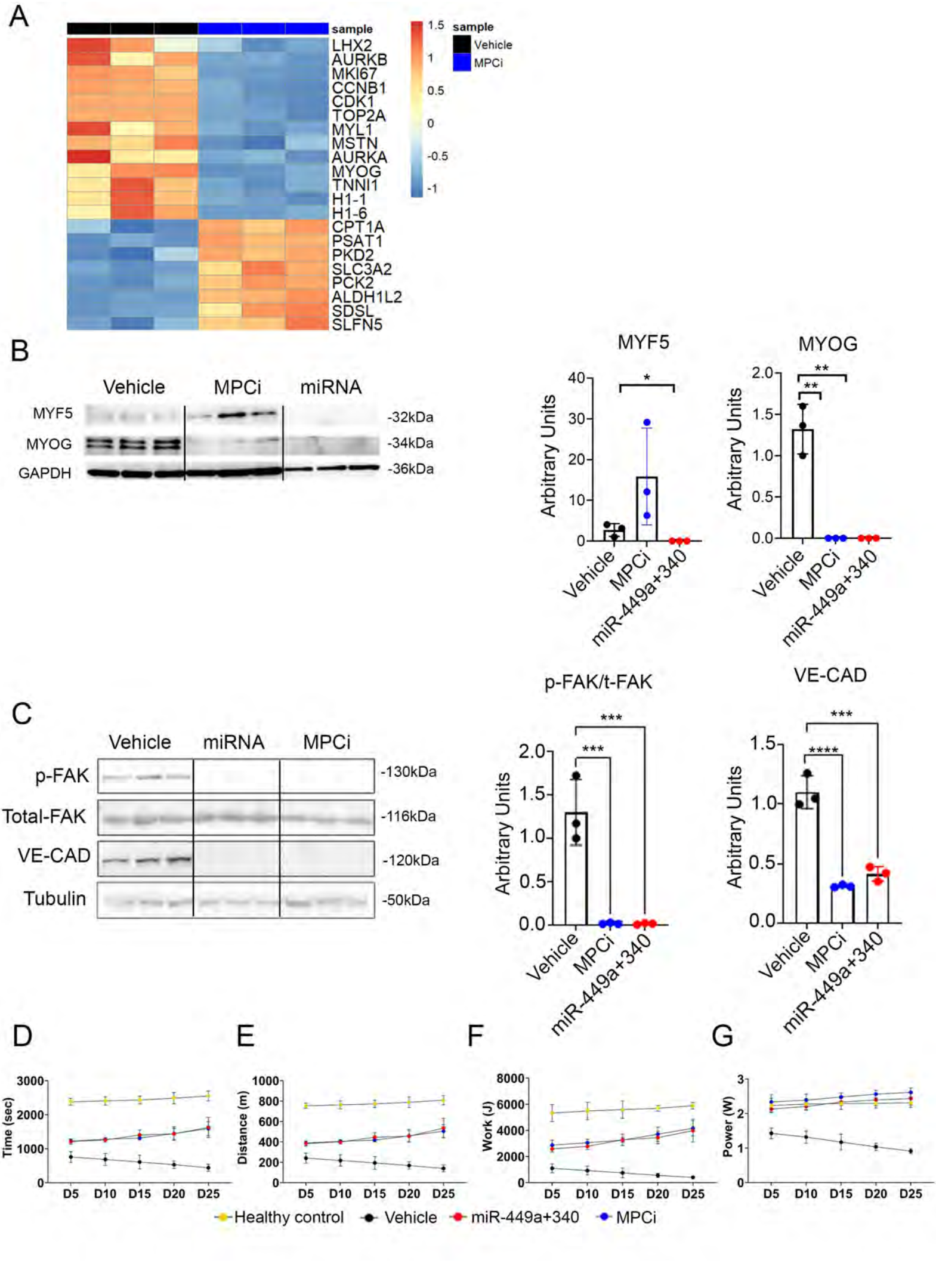
A
sample
LHX2
AURKB
MKI67
CCNB1
CDK1
TOP2A
MYL1
MSTN
AURKA
MYOG
TNNI1
H1-1
H1-6
CPT1A
PSAT1
PKD2
SLC3A2
PCK2
ALDH1L2
SDSL
SLFN5
1.5
1
0.5
0
-0.5
-1
sample
Vehicle
MPCi
B
Vehicle
MPCi
miRNA
MYF5
MYOG
GAPDH
-32kDa
-34kDa
-36kDa
MYF5
MYOG
Arbitrary Units
Vehicle
MPCi
miR-449a+340
C
Vehicle
miRNA
MPCi
p-FAK
Total-FAK
VE-CAD
Tubulin
-130kDa
-116kDa
-120kDa
-50kDa
p-FAK/t-FAK
VE-CAD
D
E
F
G
Time (sec)
Distance (m)
Work (J)
Power (W)
D5
D10
D15
D20
D25
Healthy control
Vehicle
miR-449a+340
MPCi

Figure S10. UK-5099 effects in vitro and in vivo, related to Figure 4 and Figure 5. (A) Heatmap of proteins from proteomic analysis after UK-5099 overlapping with genes differentially expressed after miR-449a+340 (n=3); (B) Western Blot and relative quantification for MYF5 and MYOG of human FN-RMS after miRNA or MPCi perturbation compared to vehicle (n=3); (C) Western Blot and relative quantification for P-FAK/Total FAK ratio and VE-Cadherin of human FN-RMS after miRNA or MPCi perturbation compared to vehicle (n=3). Data presented as mean +/- SD, one-way ANOVA. *p<0.05, **p<0.01, ***p<0.001, ****p<0.0001; (D) time (sec), (E) distance (in m), (F) work (in J), and (G) power (in W) measured during treadmill exhaustion test of tumor-bearing mice after miRNA or MPCi perturbation compared to vehicle, with age-matched sham-treated healthy C57Bl/6 mice used as control (n=6 per group). Data presented as mean +/- SD, one-way ANOVA. P-values in Table S2.

Gene	Sequence forward	Sequence reverse
CCND1	GAGGCGGAGGAGAACAAACA	GGAGGGCGGATTGGAAATGA
MDM2	TGTTTGGCGTGCCAAGCTTCTC	CACAGATGTACCTGAGTCCGATG
CCNE2	CTTACGTCACTGATGGTGCTTGC	CTTGGAGAAAGAGATTTAGCCAGG
CCND3	AGATCAAGCCGCACATGCGGAA	ACGCAAGACAGGTAGCGATCCA
CCNB2	CAACCAGAGCAGCACAAGTAGC	GGAGCCAACTTTTCCATCTGTAC
CCNG2	CTCCGGCACGATGAAGGATT	ATCATTCTCCGGGGTAGCCT
RPL13A	CCTGGAGGAGAAGAGGAAAGAGA	TTGAGGACCTCTGTGTATTTGTCAA

Table S1. Primer sequences used for qRT-PCR, related to Figure 2B

A

Sk.M Relative Flux(p/s)	D5	D10	D12	D14	D16	D18	D20	D22
Vehicle vs miR-449a+340	ns	ns	***	****	****	****	****	****
Vehicle vs. MPCi	ns	ns	***	****	****	****	****	****

B

Lung Relative Flux(p/s)	D5	D10	D12	D14	D16	D18	D20	D22
Vehicle vs miR-449a+340	ns	ns	***	****	****	****	****	****
Vehicle vs. MPCi	ns	ns	***	****	****	****	****	****

C

Time (sec)	D5	D10	D15	D20	D25
Healthy Ctrl vs Vehicle	***	***	***	****	****
Healthy Ctrl vs miR-449a+340	**	**	**	**	ns
Healthy Ctrl vs MPCi	**	**	*	**	*
Vehicle vs miR-449a+340	**	***	***	**	*
Vehicle vs MPCi	**	***	***	**	**
miR-449a+340 vs MPCi	ns	ns	ns	ns	ns

D

Distance (m)	D5	D10	D15	D20	D25
Healthy Ctrl vs Vehicle	***	***	***	****	****
Healthy Ctrl vs miR-449a+340	**	**	**	**	ns
Healthy Ctrl vs MPCi	**	**	*	**	*
Vehicle vs miR-449a+340	**	***	***	**	*
Vehicle vs MPCi	**	***	***	**	**
miR-449a+340 vs MPCi	ns	ns	ns	ns	ns

E

Work (J)	D5	D10	D15	D20	D25
Healthy Ctrl vs Vehicle	***	***	***	****	****
Healthy Ctrl vs miR-449a+340	**	**	**	**	ns
Healthy Ctrl vs MPCi	**	**	*	**	*
Vehicle vs miR-449a+340	**	***	***	**	*
Vehicle vs MPCi	**	***	***	**	**
miR-449a+340 vs MPCi	ns	ns	ns	ns	ns

F

Power (W)	D5	D10	D15	D20	D25
Healthy Ctrl vs Vehicle	***	***	***	****	****
Healthy Ctrl vs miR-449a+340	**	**	**	**	ns
Healthy Ctrl vs MPCi	**	**	*	**	*
Vehicle vs miR-449a+340	**	***	***	**	*
Vehicle vs MPCi	**	***	***	**	**
miR-449a+340 vs MPCi	ns	ns	ns	ns	ns

Table S2. P-values related to Figure 5 from the relative photon flux (pulse/sec) of the ROIs from (A) primary tumor, (B) lungs *in vivo* and (C) lungs *ex vivo*; P-values related to Figure S10 from treadmill exhaustion test measured in (D) distance, (E) work and (F) power.